

High Intensity RF Linear Accelerators

2.4 Low Energy Beam Transport for Intense Beams

Yuri Batygin

Los Alamos National Laboratory

U.S. Particle Accelerator School

Albuquerque, New Mexico, 23 – 27 June 2014

Content

LEBT Functions and Requirements

Ion Sources

Thermal Beam Emittance in Particle Sources

Space Charge Effects in the Extraction Region of Particle Sources Child-Langmuir Law

Ion Sources Extraction Geometry

Electrostatic versus Magnetostatic LEBT

Space Charge Neutralization in LEBT

Design of Magnetostatic LEBT

Separation of Beam Components in LEBT

Beam Chopping

Beam Matching in LEBT

LEBT Functions and Requirements

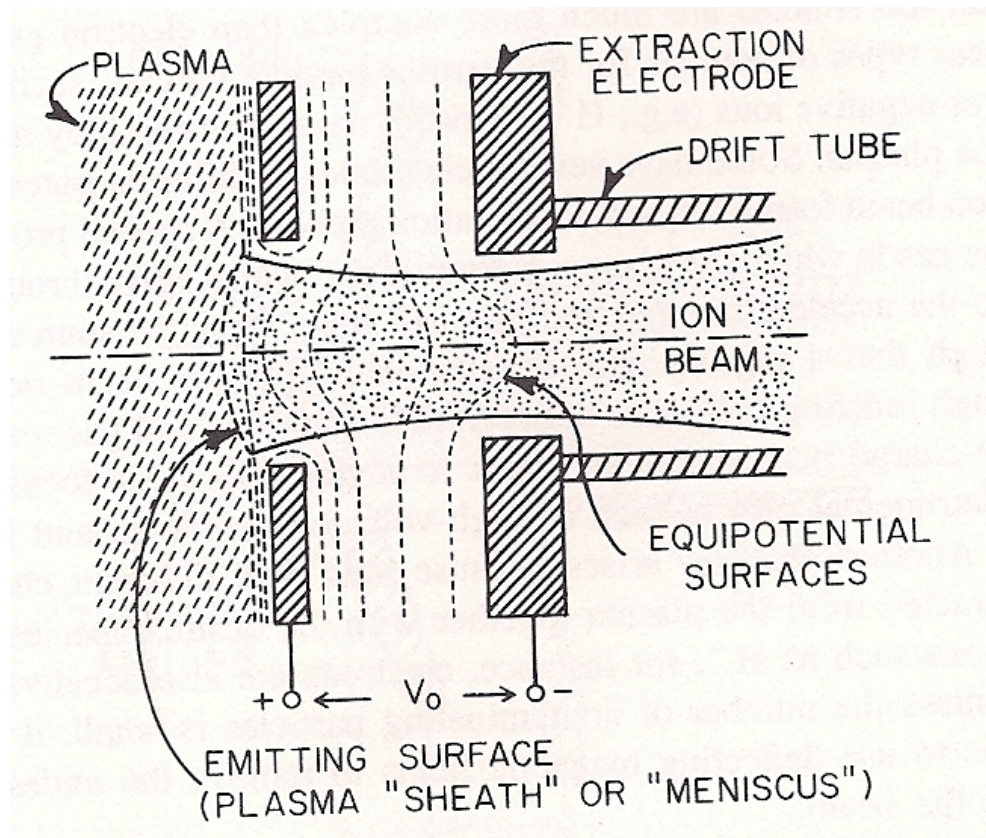
LEBT Purposes:

- Extraction and low – energy acceleration of the beam
- Match beam out of the ion source to the transport channel
- Dispose of electrons emitted along with the ions
- Match beam into the RF Accelerator (RFQ)
- Provide beam diagnostics and test facilities
- Provide fast switching (chopping) before the RF Accelerator to introduce time structure of the beam

Beam Physics Issues:

- Electrostatic vs magnetostatic LEBT
- Minimization of emittance growth
- Beam space charge compensation
- Short neutralization time

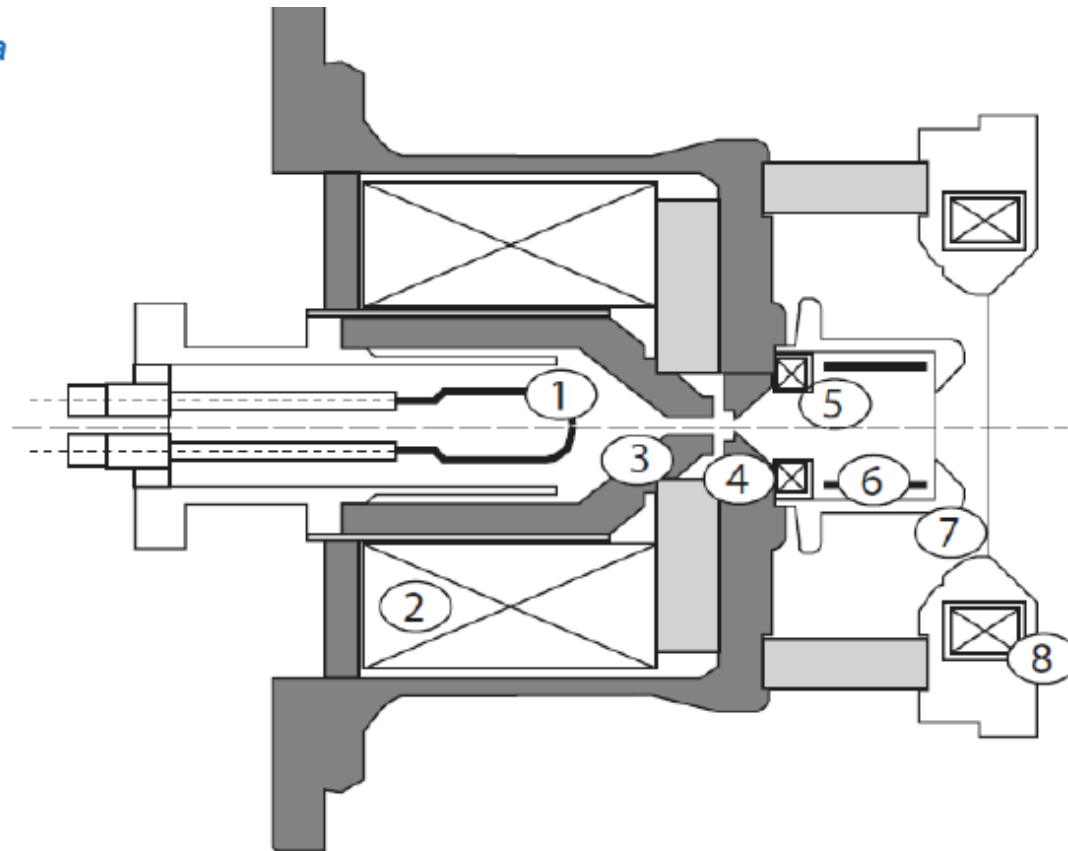
Ion Sources



Schematics of a plasma ion source (from M.Reiser, 1994.)

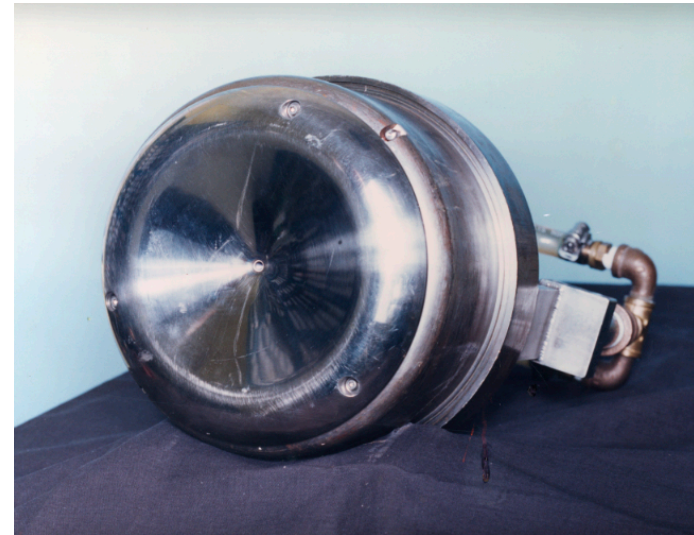
Duoplasmatron

M. A. Hone, CERN Geneva



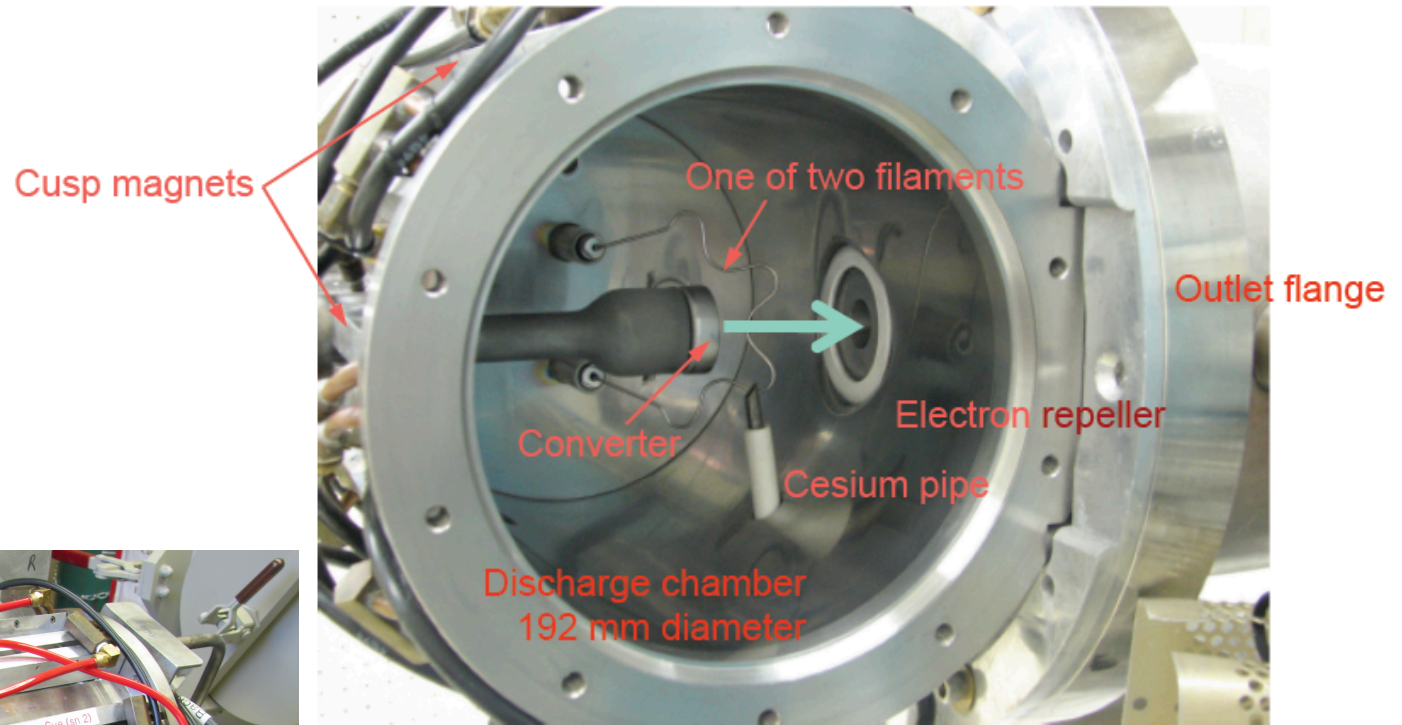
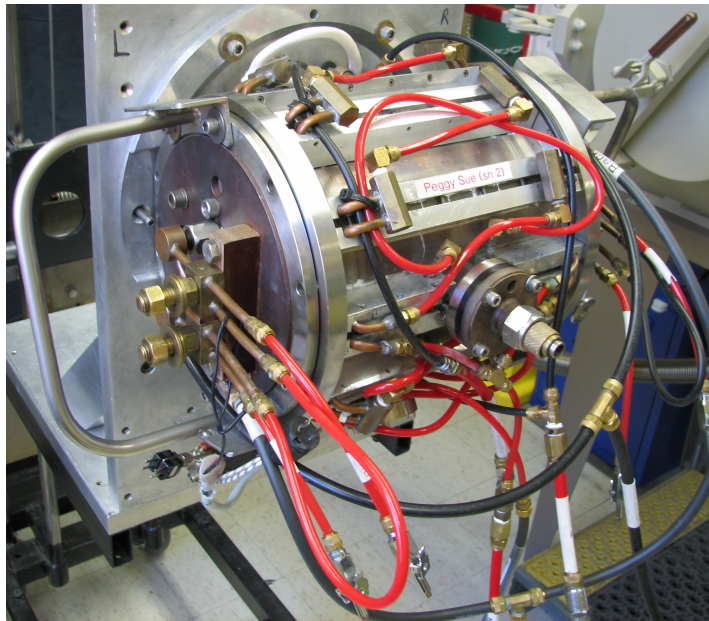
1: Oxide cathode. 2: Main magnet coil. 3: Intermediate electrode. 4: Anode with 0.6-mm aperture. 5: Auxiliary magnet coil. 6: Potential plate. 7: Expansion cup with 20-mm aperture. 8: Current transformer. Light shaded: Insulator. Dark shaded: Main magnet yoke.

LANSCCE Duoplasmatron



Side view of assembled LANSCE duoplasmatron ion source with Pierce electrode.

LANSCCE H⁻ Ion Source



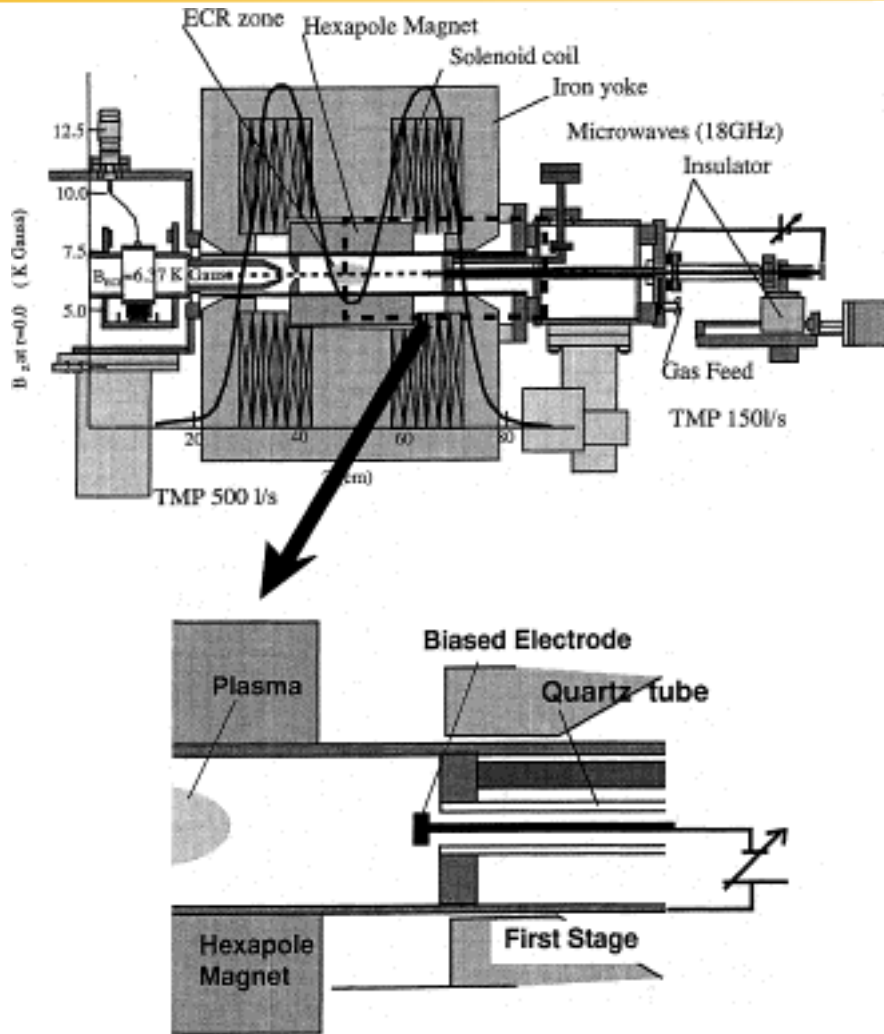
Multi-cusp bucket source with cesiated converter

H⁻ Ion Source Parameters

TABLE I
LIST OF ACCELERATOR H⁻ ION SOURCES ALONG WITH THE RELEVANT
PARAMETER SPACE DISCUSSED WITHIN THIS REVIEW. TYPICAL I_{H⁻}
CURRENTS ARE GIVEN WITH AN ASSOCIATED EMITTANCE. [13], [14] WERE
USED TO FILL IN VALUES NOT PREVIOUSLY CITED. UNDERLINED PARAMETERS
ARE FROM [13] AND BRACKETED PARAMETERS ARE FROM [14]

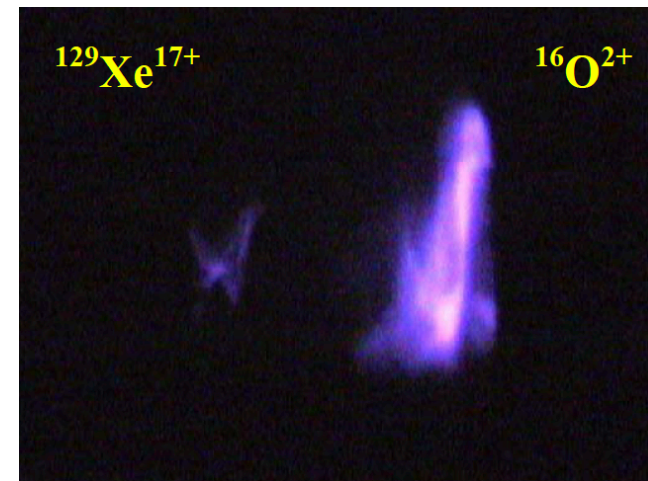
Source Type (drive)	Source Location	I _{H⁻} (ma)	Beam df (%)	Rep. Rate (Hz)	ϵ_{rms} x/y (π mm-mrad)	P _d (kW)	e/H ⁻	Life-time (month)
Multicusp Volume, H₂								
RF	DESY (HERA)	40	0.12	8	0.25	~20	26	> 12
LaB ₆ fil.	J-PARC (KEK)	38	0.9	25		35		
Multicusp Volume, Cs+H₂								
RF	SNS	33	6.0	60	0.22/0.18	~40		
W fil.	TRIUMF	20	100	dc	0.022	~5	4-5	~?
W fil.	J-PARC (JAERI)	72	5.0	50	0.13/0.15			
SPS								
Magnetron	BNL	100	0.5	7.5	0.4	~2	0.5	<u>~6</u>
	Fermilab	60	0.1	15	0.2/0.3	~7		~6
	DESY	50	<u>0.05</u>	<u>6</u>	0.46/0.31	{~5}		<u>~9</u>
Penning	ISIS	45	1.0	50	0.6/0.7	<u>4</u>		~2
	INR	50	2.0	100	0.4/0.7 ($\epsilon_{n,F7}$)	{~10}		<u>~0.5</u>
Hollow cath.	BINP	8	100	dc	0.2/0.3	0.4		<u>~0.2</u>
Converter (W fil.)	LANSCE	17	12.0	120	0.13	~6	2.5	~1
(LaB ₆ fil.)	KEK	20	0.5	20	0.33	~4	4.5	3-4

Electron-Cyclotron Resonance (ECR) Ion Source



Cross sectional view of RIKEN 18 GHz ECRIS (T.Nakagawa et al, NIM-A 396, p.9 (1997))

ECR resonance condition: $\omega_c = \omega_{RF}$



2D image of the $^{129}\text{Xe}^{17+}$ ion beam of the energy of 255 keV and current of 12 e μ A extracted from the mVINIS Ion Source, together with the image of the $^{16}\text{O}^{2+}$ beam.

Thermal Beam Emittance in Particle Sources

The ultimate goal of accelerator designers is to minimize emittance as much as possible. An intrinsic limitation of beam emittance in particle sources comes from the finite value of plasma temperature in an ion source, or the finite value of cathode temperature in an electron source. Equilibrium thermal particle momentum distribution in these sources is in fact, close to the Maxwell distribution:

$$f(p) = n \left(\frac{m}{2\pi kT} \right)^{3/2} \exp \left(- \frac{p^2}{2mkT} \right)$$

Rms value of mechanical momentum is

$$\langle p_x^2 \rangle = mkT$$

Beam radius is usually adopted to be double the root-mean-square beam size, $R = 2 \sqrt{\langle x^2 \rangle}$. Fortunately, for particle sources, one can assume that $\langle x p_x \rangle = 0$ because there is no correlation between particle position and particle momentum. Therefore, the normalized emittance of a beam, extracted from a particle source, is

$$\varepsilon = 2R \sqrt{\frac{kT}{mc^2}}$$

Some sources can be operated only in presence of a longitudinal magnetic field, which produces an additional limitation on the value of the beam emittance. For instance, in an electron-cyclotron-resonance (ECR) ion source, charged particles are born in a longitudinal magnetic field B_z , fulfilling the ECR resonance condition $2\omega_L = \omega_{RF}$, where ω_L is the Larmor frequency of electrons and ω_{RF} is the microwave frequency. Canonical momentum of an ion, $P_x = p_x - qA_x$, in a longitudinal magnetic field B_z is:

$$P_x = p_x - q \frac{B_z y}{2}$$

The rms value of canonical momentum is given by:

$$\langle P_x^2 \rangle = \langle p_x^2 \rangle - q B_z \langle p_x y \rangle + \frac{q^2 B_z^2}{4} \langle y^2 \rangle$$

The first term describes the thermal spread of mechanical momentum of ions in plasma, and is given by $\langle p_x^2 \rangle = mkT$. The middle term equals zero because there is no correlation between p_x and y inside the source. The last term is proportional to the rms value of the transverse coordinate $\langle y^2 \rangle = R^2/4$. As a result, we can rewrite $\langle P_x^2 \rangle$ as follows:

$$\langle P_x^2 \rangle = \langle p_x^2 \rangle + \left(\frac{q B_z R}{4} \right)^2$$

The normalized beam emittance ε , extracted from the source is

$$\varepsilon = 2R \sqrt{\frac{kT_i}{mc^2} + \left(\frac{qB_z R}{4mc}\right)^2}$$

Therefore, the presence of a longitudinal magnetic field at the source acts to increase the value of the beam emittance.

Additional sources contributing to beam emittance :

- irregularities in the plasma meniscus extraction surface
- aberrations due to ion-source extraction optics
- optical aberrations of the focusing elements of the LEBT
- non-linearity of the electric field created by the beam space charge
- beam fluctuations due to ion-source instability or power regulation

Space Charge Effects in the Extraction Region of Particle Sources: Child-Langmuir Law

2.5.2 *

Planar Diode with Space Charge (Child-Langmuir Law)

Let us now include the effect of the space charge of the electron current in the diode on the potential distribution and electron motion. To simplify our analysis, we assume that all electrons are launched with initial velocity $\mathbf{v}_0 = 0$ from the cathode (i.e., they are moving on straight lines in the x -direction). This is an example of *laminar flow* where electron trajectories do not cross and the current density is uniform. We try to find the steady-state solution ($\partial/\partial t = 0$) in a self-consistent form. The electrostatic potential is determined from the space-charge density ρ via Poisson's equation, with $\phi = 0$, at $x = 0$ and $\phi = V_0$ at $x = d$, as in the previous case. The relationship between ρ , the current density \mathbf{J} , and the electron velocity \mathbf{v} follows from the continuity equation ($\nabla \cdot \mathbf{J} = 0$ or $\mathbf{J} = \rho\mathbf{v} = \text{const}$). The velocity in turn depends on the potential ϕ and is found by integrating the equation of motion. Thus we have the following three equations:

$$\nabla^2 \phi = \frac{d^2 \phi}{dx^2} = -\frac{\rho}{\epsilon_0} \quad (\text{Poisson's equation}), \quad (2.129)$$

$$J_x = \rho \dot{x} = \text{const} \quad (\text{continuity equation}), \quad (2.130)$$

$$\frac{m}{2} \dot{x}^2 = e\phi(x) \quad (\text{equation of motion}). \quad (2.131)$$

*From M.Reiser, Theory and Design of Charged Particle Beams, Wiley, 1994

Substituting $\dot{x} = [2e\phi(x)/m]^{1/2}$ from (2.131) into (2.130) and $\rho = J_x/\dot{x}$ from (2.130) into (2.129) yields

$$\frac{d^2\phi}{dx^2} = \frac{J}{\epsilon_0(2e/m)^{1/2}} \frac{1}{(\phi)^{1/2}}, \quad (2.132)$$

where the current density $J = -J_x$ is defined as a positive quantity. After multiplication of both sides of Equation (2.132) with $d\phi/dx$, we can integrate and obtain

$$\left(\frac{d\phi}{dx}\right)^2 = \frac{4J}{\epsilon_0(2e/m)^{1/2}} \phi^{1/2} + C. \quad (2.133)$$

Now $\phi = 0$ at $x = 0$, and if we consider the special case where $d\phi/dx = 0$ at $x = 0$, we obtain $C = 0$. A second integration then yields (with $\phi = V_0$ at $x = d$)

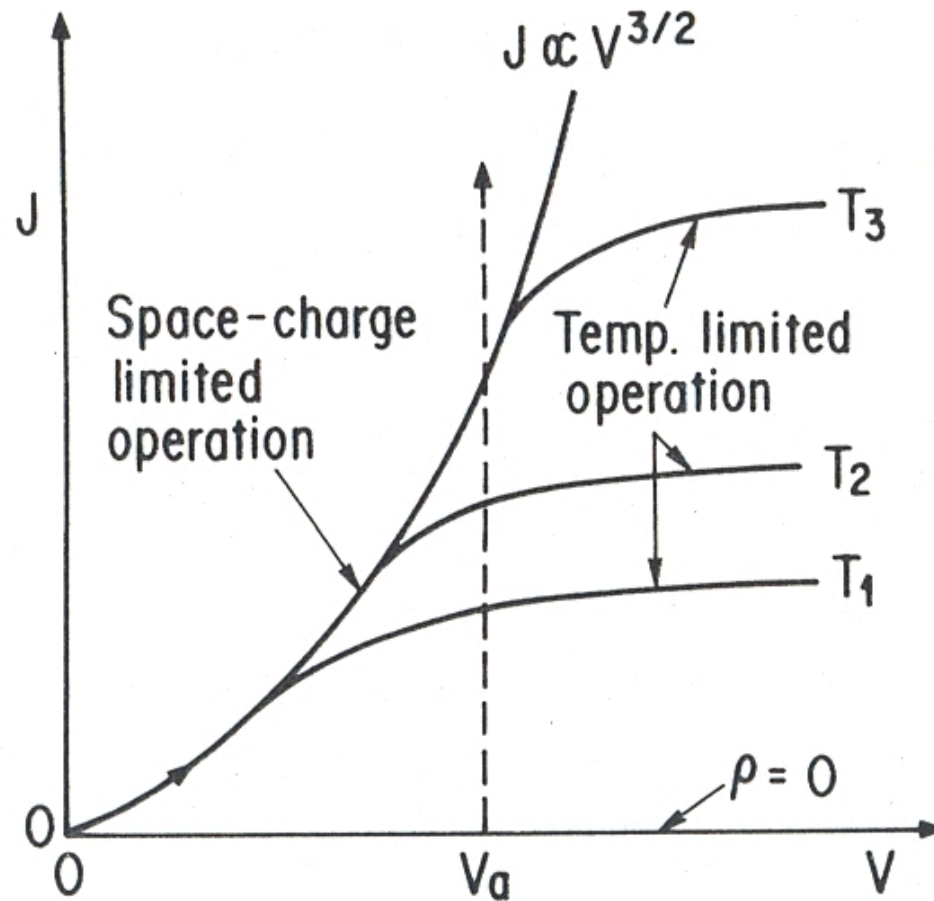
$$\frac{4}{3}\phi^{3/4} = 2\left(\frac{J}{\epsilon_0}\right)^{1/2} \left(\frac{2e}{m}\right)^{-1/4} x,$$

or

$$\phi(x) = V_0 \left(\frac{x}{d}\right)^{4/3}. \quad (2.134)$$

with the relation

$$J = \frac{4}{9}\epsilon_0 \left(\frac{2e}{m}\right)^{1/2} \frac{V_0^{3/2}}{d^2}. \quad (2.135)$$



Current-voltage relation at constant cathode temperature (from S.Isagawa, Joint Accelerator School, 1996).

In ion sources, the shape of plasma meniscus is determined by the balance between plasma pressure and applied electrostatic voltage for ion extraction.

To determine shape of plasma meniscus, let us consider self-consistent problem for the beam extracted from spherical emitter of radius R_1 (plasma) and spherical collector of radius R_2 ($R_2 < R_1$). Saturated current density extracted from the plasma

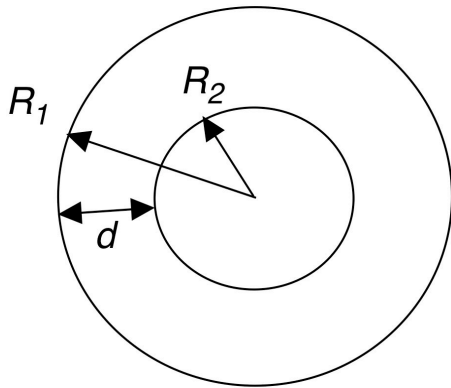
$$j = n_i e \sqrt{\frac{kT_e}{m_i}}$$

We will assume that all particle have the same extracted velocities, so the current density is $j = \rho v_r$ and particle velocity is

$$v_r = \sqrt{\frac{2qU}{m}}$$

where U is the potential between two spheres. Therefore, beam space charge density is

$$\rho = \frac{j}{\sqrt{\frac{2qU}{m}}}$$



On derivation of Child-Langmuir law between spherical surfaces.

Let us substitute space charge density into Poisson's equation in spherical coordinates:

$$\frac{1}{r^2} \frac{d}{dr} \left(r^2 \frac{dU}{dr} \right) = -\frac{1}{\epsilon_o} \frac{j}{\sqrt{\frac{2qU}{m}}}$$

Solution of Poisson's equation for concentric spheres is

$$\frac{j}{U^{3/2}} = \frac{4\sqrt{2}}{9} \epsilon_o \sqrt{\frac{q}{m}} \frac{1}{R_1^2 \alpha^2}$$

where $\alpha = Y - 0.3Y^2 + 0.075Y^3$, $Y = \ln \frac{R_2}{R_1}$

This is the Child-Langmuir law for spherical surfaces. When the distance between emitter and collector is much smaller than the raduses $d = R_1 - R_2 \ll R_1$, the following approximations can be used:

$$Y = \ln\left(\frac{R_1 - d}{R_1}\right) \approx -\frac{d}{R_1} - \frac{1}{2}\left(\frac{d}{R_1}\right)^2 - \frac{1}{2}\left(\frac{d}{R_1}\right)^3$$

$$\frac{1}{R_1^2 \alpha^2} \approx \frac{1}{d^2} \left(1 - 1.6 \frac{d}{R_1}\right)$$

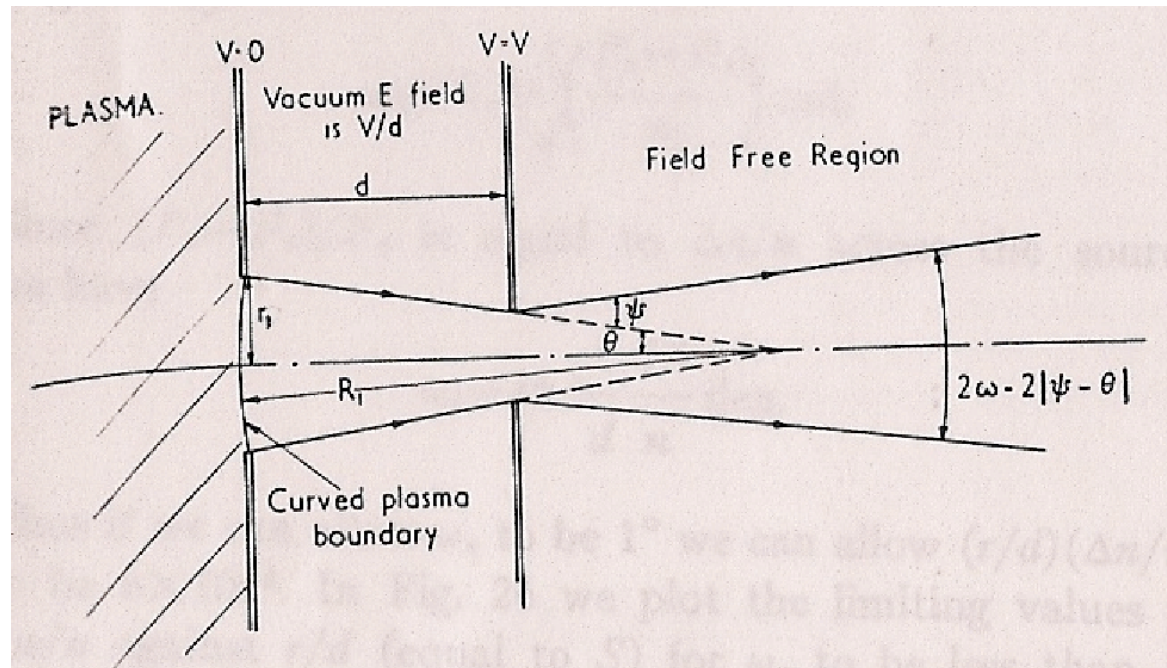
With this approximation, Child-Langmuir law is expressed as

$$\frac{j}{U^{3/2}} = \frac{4\sqrt{2}}{9} \epsilon_o \sqrt{\frac{q}{m}} \frac{1}{d^2} \left(1 - 1.6 \frac{d}{R_1}\right)$$

Let us apply now obtained result to the problem of plasma beam extraction from small extraction hole of the radius R_{ext} . From Fig the relationship between extraction radius R_{ext} and radius R_l is

$$R_l = \frac{r_1}{\sin \theta} \approx \frac{r_1}{\theta}$$

where θ is associated with initial beam slope.



Scheme of simplified ion optics in beam extraction region (J.R.Coupland et al., Rev. Sci. Instruments, Vol. 44, No 9, (1973), p.1258.

Beam current density

$$j = \frac{I}{\pi r_1^2}$$

Substitution of expression for beam current density into Child-Langmuir law reads:

$$\frac{I}{U^{3/2}} = \frac{4\sqrt{2}\pi}{9} \epsilon_o \sqrt{\frac{q}{m}} \left(\frac{r_1}{d}\right)^2 \left(1 - 1.6 \frac{d}{r_1} \theta\right)$$

Beam perveance:

$$P_b = \frac{I}{U^{3/2}}$$

Child-Langmuir perveance of one dimensional diode

$$P_o = \frac{4\sqrt{2}\pi}{9} \epsilon_o \sqrt{\frac{q}{m}} \left(\frac{r_1}{d}\right)^2$$

Extracted beam slope (plasma meniscus):

$$\theta = 0.625 \frac{r_1}{d} \left(\frac{P_b}{P_o} - 1\right)$$

If $P_b \ll P_o$, it corresponds to the extracted beam with negligible intensity, and initial convergence of the beam is defined by extraction geometry only

$$\theta = -0.625 \frac{r_1}{d}$$

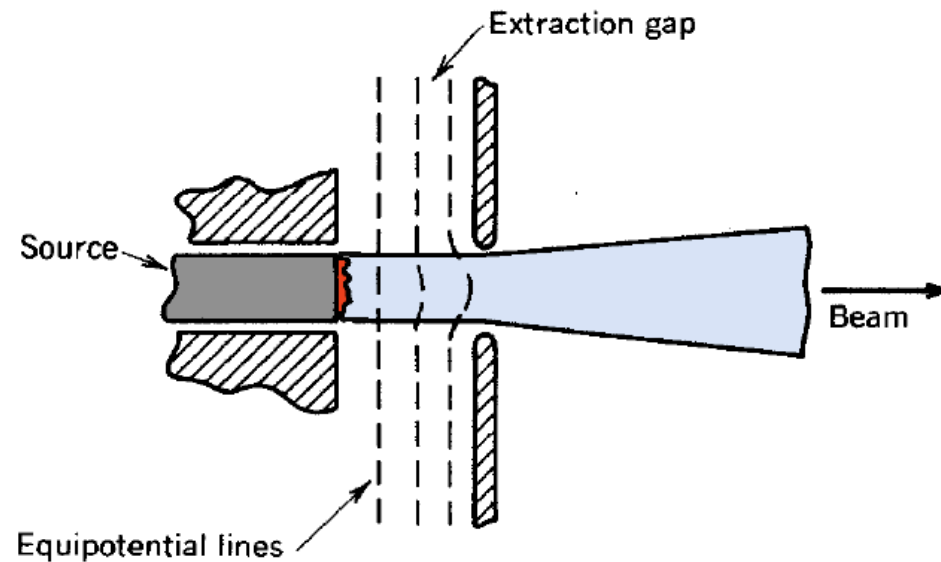
According to Child-Langmuir law, the potential inside extraction gap has the following z-dependence:

$$U(z) = U_{\text{ext}} \left(\frac{z}{d_{\text{ext}}} \right)^{4/3}$$

Inside extraction gap particles move in the field, which, in the first approximation, has only longitudinal component

$$E_z = \frac{4}{3} U_{\text{ext}} \frac{z^{1/3}}{d_{\text{ext}}^{4/3}}$$

Outside extraction gap the field drops to zero.



Extraction gap showing defocusing effect (S.Humphries, 1999).

Due to equation $\text{div } \vec{E} = \frac{1}{r} \frac{\partial}{\partial r}(r E_r) + \frac{\partial E_z}{\partial z} = 0$

any change in longitudinal field results in appearance of transverse field component, which (in this case) defocuses beam:

$$E_r = -\frac{1}{r} \int_0^r \frac{\partial E_z}{\partial z} r' dr' \approx -\frac{r}{2} \frac{\partial E_z}{\partial z}$$

Equation of particle motion: $\frac{d^2 r}{dz^2} = -\frac{q}{mv_z^2} r \frac{1}{2} \frac{\partial E_z}{\partial z}$

Slope of particle trajectory at the exit of the gap:

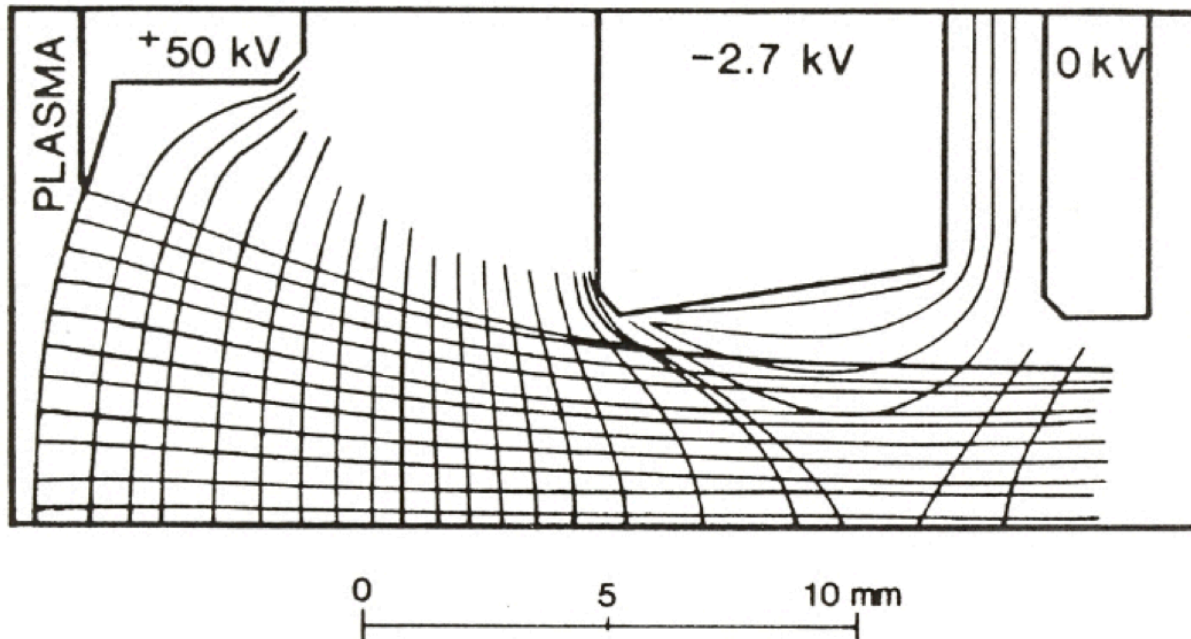
$$\psi = \Delta\left(\frac{dr}{dz}\right) = -\frac{q}{2mv_z^2} r \int \frac{\partial E_z}{\partial z} dz = \frac{q}{2mv_z^2} r E_z = \frac{r E_z}{4U_{ext}} = \frac{r}{3d}$$

Finally, divergence of the extracted beam is as follows:

$$\omega = |\theta + \psi| = \left| 0.625 \frac{r_1}{d} \left(\frac{P_b}{P_o} - 1 \right) + \frac{r_1}{3d} \right| = \left| 0.29 \frac{r_1}{d} \left(1 - 2.14 \frac{P_b}{P_o} \right) \right|$$

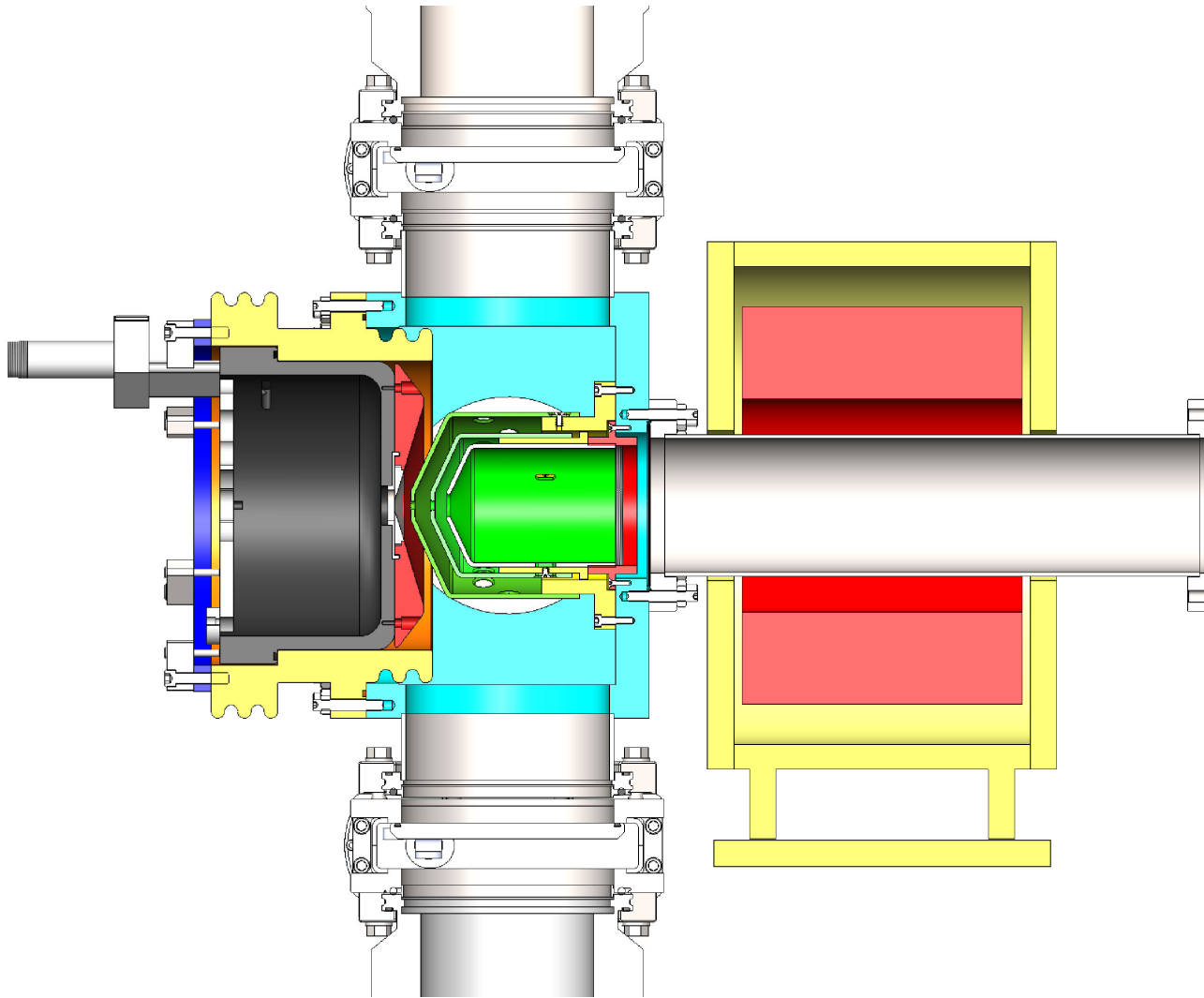
Repeller Electrode

- Extraction electric field is attractive for neutralizing particles resulting in beam decompensation
- Repelling electrode (trapping electrode) is inserted upstream of the extraction electrode. This electrode creates a potential barrier to keep the neutralizing particles within the beam by preventing them to be attracted toward the ion source.



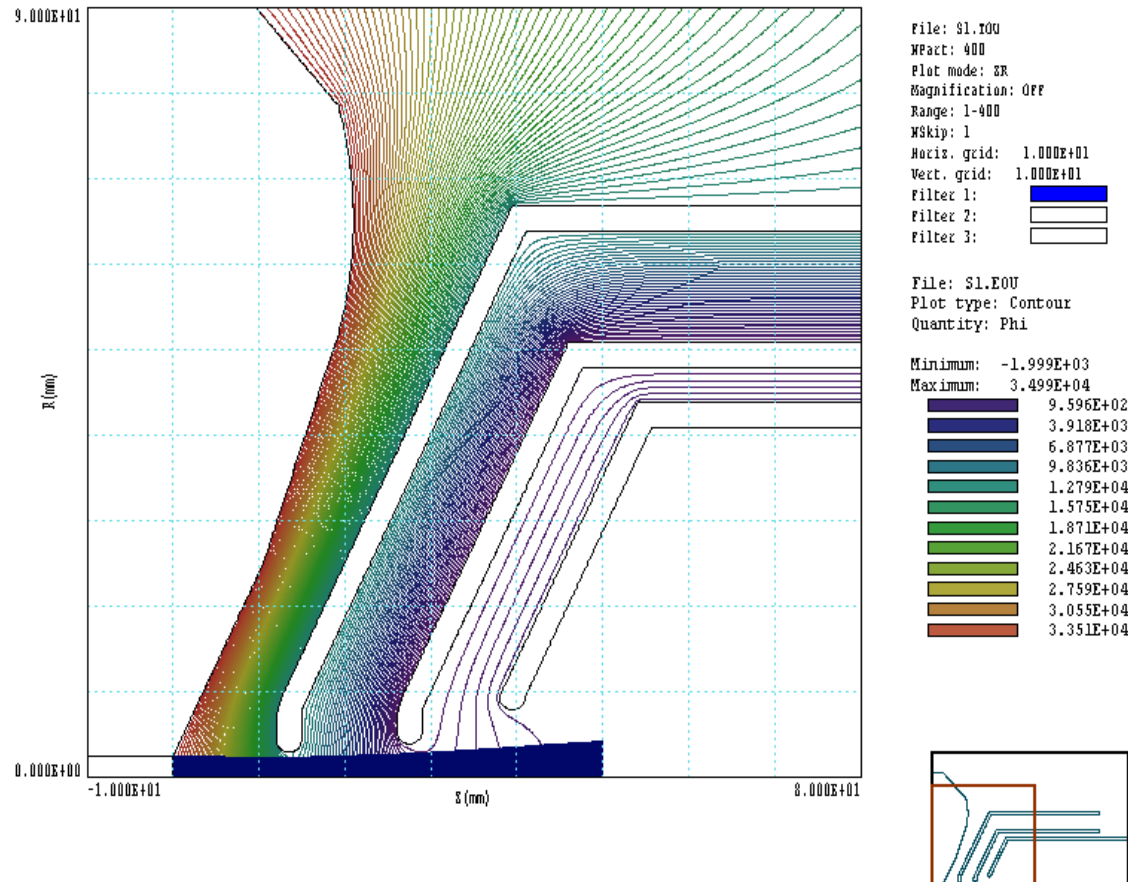
Three electrode beam extraction system (B.Piosczyk, FZ Karlsruhe).

Four-Electrode Extraction System



Layout of ion source and extraction system. Duoplasmatron source is on the left. Extraction electrodes are in the center and the 1st LEBT solenoid is on the right. Pumps are above and below electrodes.

Beam Extraction from 4 - Electrode Extraction Geometry



Electrode geometry and beam extraction for a 35 keV, 18 mA H⁺ beam.

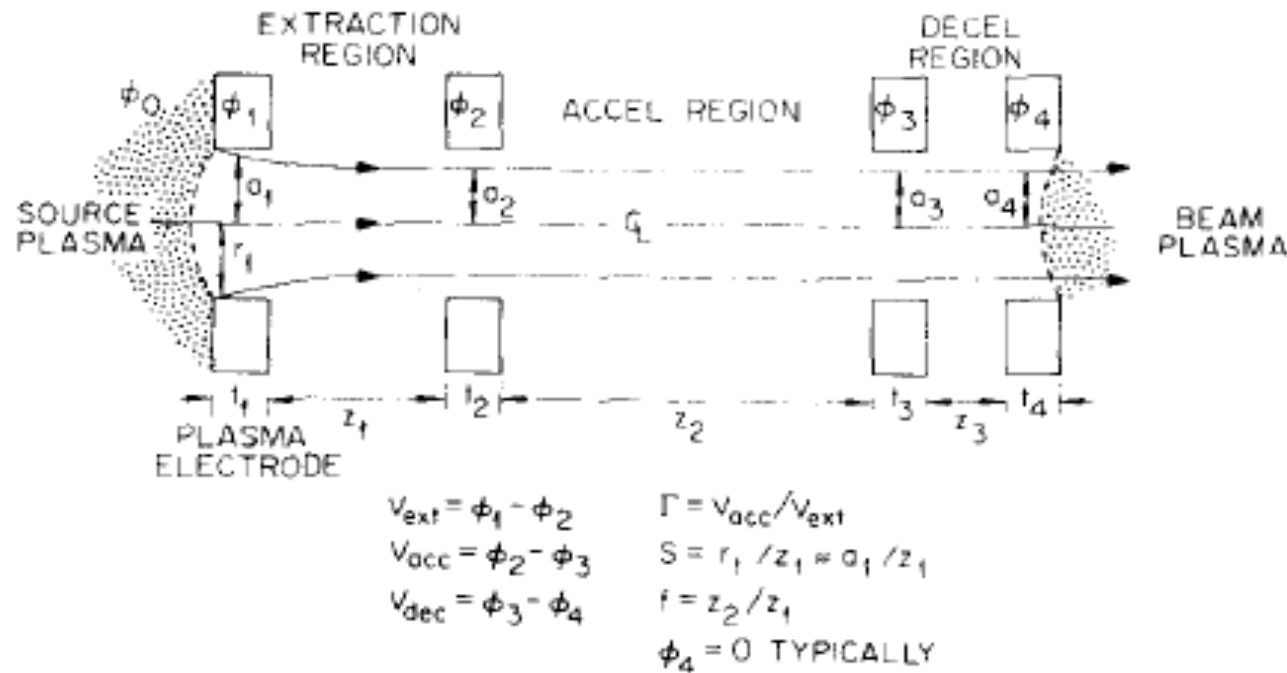


FIG. 1. Schematic of a two-stage four-electrode accelerating column with definitions of some relevant parameters and nomenclature.

$$\theta = 0.62S \left[\frac{P}{P_0} - 0.40 \left(\frac{a_2}{a_1} \right) \frac{\Gamma^2}{f(1+\Gamma)} + 0.53 \left(\frac{a_2}{a_1} \right) - 1 \right] + 0.31S \left(\frac{P}{P_0} \right) \left[1 + \left(\frac{t_1}{t_2} \right) + 0.35 \left(\frac{a_1}{a_2} \right) \times \left(f + \frac{z_3 + t_2 + t_3}{z_1} \right) (1 + 0.50\Gamma)^{-1.5} \right].$$

where P is the perveance in the extraction gap, $P = I / V_{ext}^{3/2}$ and P_0 is the Child-Langmuir⁷ space-charge-limited perveance for the one-dimensional diode of length z_1 with no electrons, $P_0 = \left(\frac{4}{3} \pi \right) (a_1^2 / z_1^2) \epsilon_0 (2e/M)^{1/2}$, where ϵ_0 is the permittivity of the vacuum.

Nonlinear Effects in Beam Optics (Lejeune, 1983)

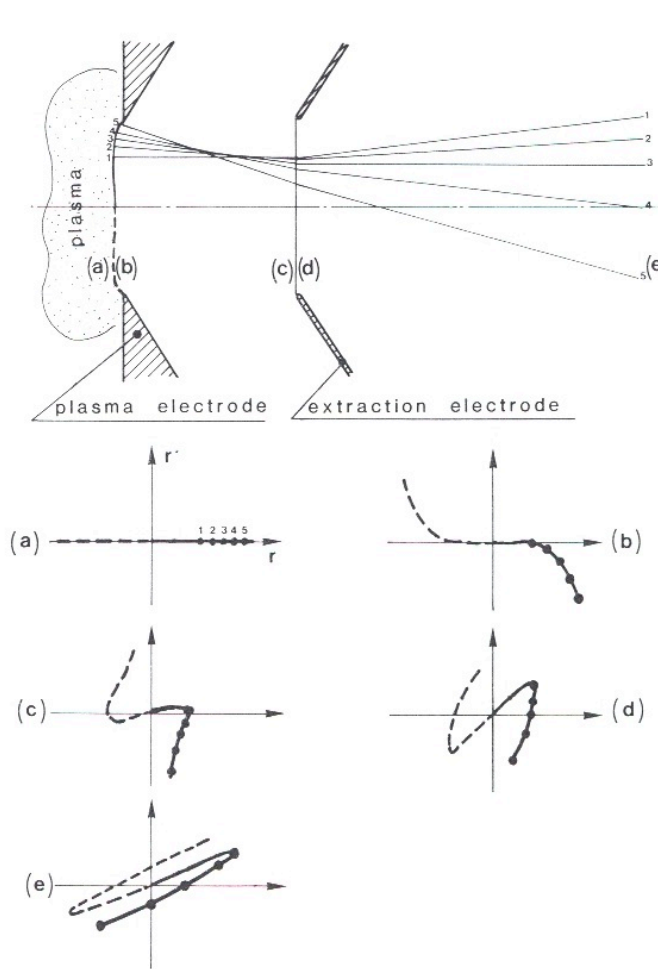


FIG. 24. Schematic illustration of the mechanism that produces an S-shaped emittance pattern for the beam emergent from an extraction optics if the radius of curvature of the plasma meniscus is not uniform. In the upper part of the figure are shown particular trajectories normally emitted from the rim of the plasma meniscus, where the radius of curvature varies strongly. In the lower diagrams the evolution of the beam emittance pattern is shown for several meaningful cross sections: (a) in the emitter section if the plasma meniscus is planar and without transverse thermal spread, (b) after the action of the concave plasma meniscus, (c) in the entrance plane of the extraction lens, (d) in the exit plane of this lens, and (e) in the probing section after a drift.

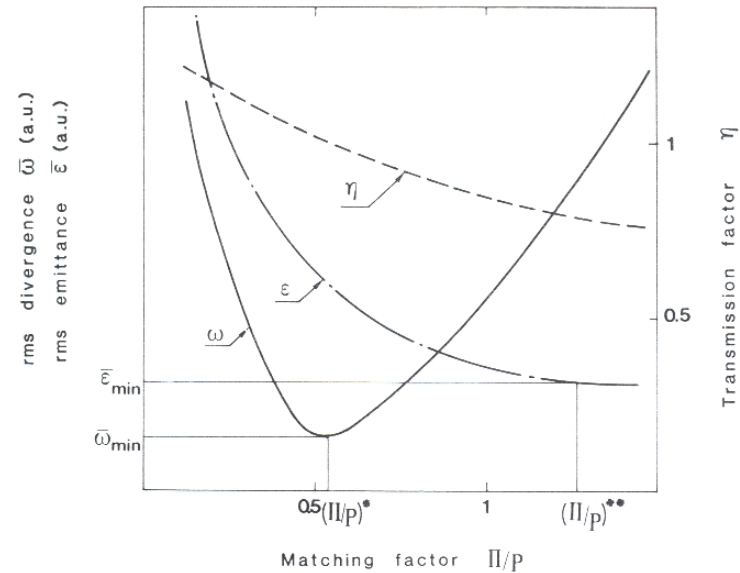


FIG. 32. Schematic representation of the three main graphs which characterize the performance of a triode extraction optics: rms divergence ($\bar{\omega}$), rms emittance ($\bar{\epsilon}$), and transmission factor ($\bar{\eta}$) as functions of the matching factor (Π/P). These graphs may be summarized by the minimum values of $\bar{\omega}$ and $\bar{\epsilon}$ and the respective optimal values of Π/P , as well as by the sensitivity factor Q , the definition of which is illustrated in Fig. 21.

Nonlinear Optics: Simulations (Whealton et. al, 1980)

244

CLAUDE LEJEUNE

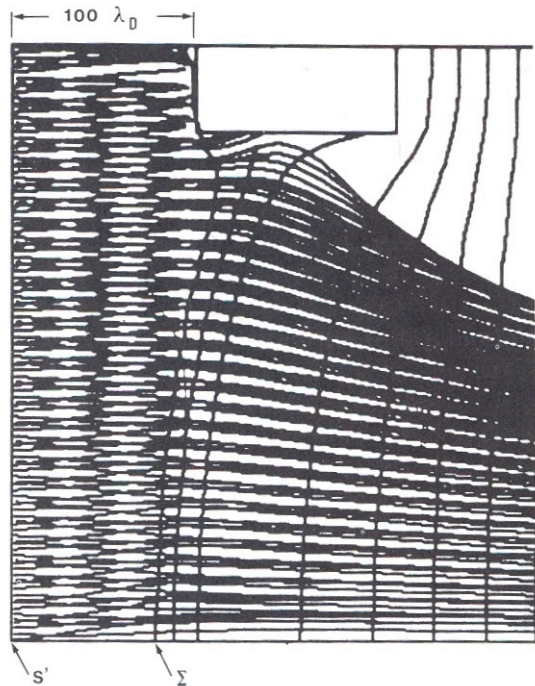


FIG. 11. Equipotential contours and ion trajectories in the region of the classical sheath edge Σ of a triode extraction optics. They are obtained from the ORNL nonlinear theory and code C (see text) (courtesy of Whealton and Whitson, 1980, and Gordon and Breach). The emissive surface (S') equivalent to the plasma is represented by the linear line on the left of the figure. The leftmost potential contour is halfway between the plasma and the screen potential and is illustrative of the position of the classical sheath edge Σ . The second contour just to the right of this is at the screen potential, and the third is at four times the difference between the plasma and the screen.



FIG. 4. Ion trajectories and potential distributions for a converged solution to Eqs. (9)–(12) showing the source-plasma sheath and nonlinear aberrations near the plasma electrode: $\delta = 0.75$, $\Gamma = 4$, and $j = 0.45j_0$.

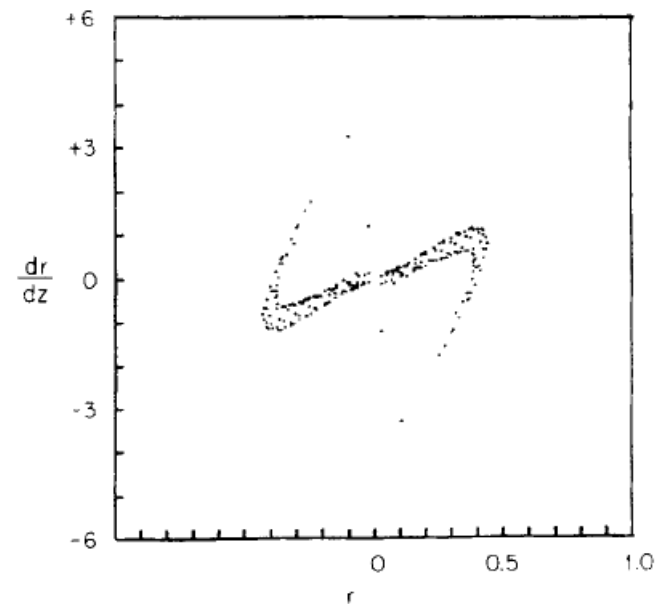


FIG. 5. Emittance diagram showing the slope and the position of exiting orbits for the case shown in Fig. 4.

Experimental Analysis of Extracted Beam Emittance (J.Aubert et al, 1983)

Beam-plasma interface and beam emittance

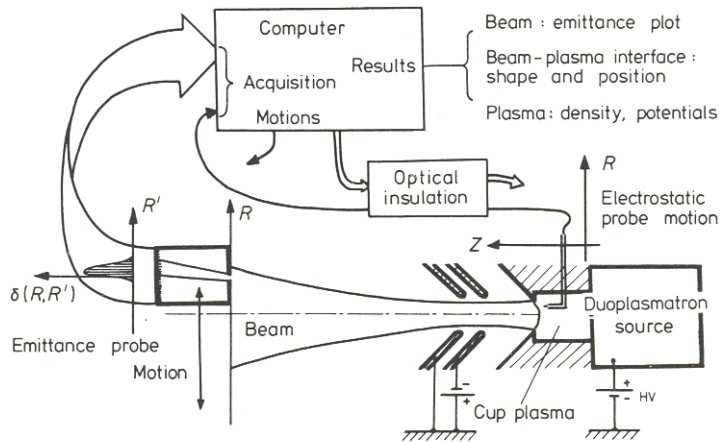


Figure 2. Principle of the computer-controlled experimental set-up.

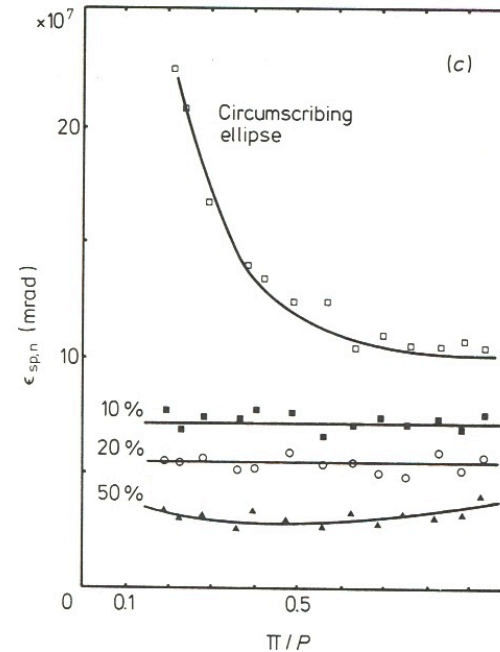
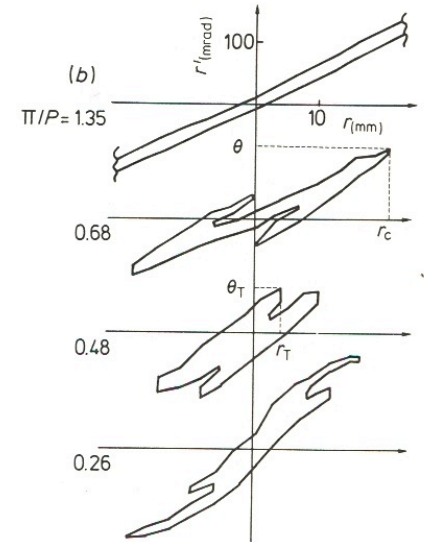
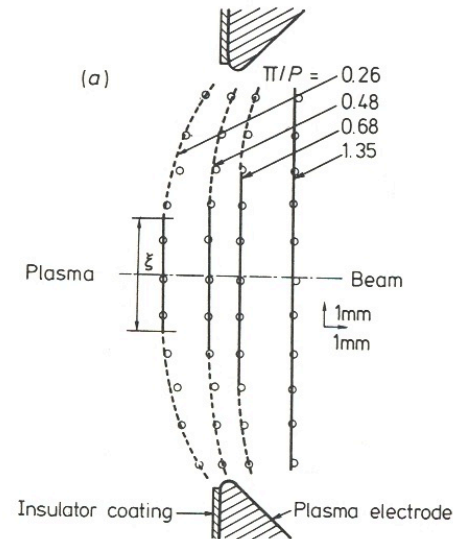
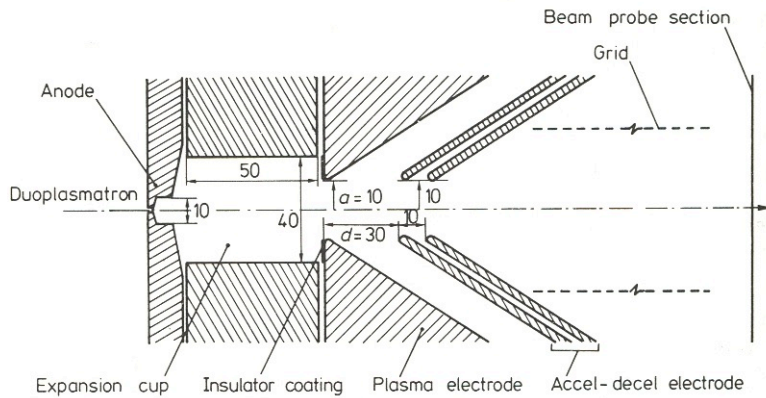


Figure 3. Beam-plasma interface for different values of the dimensionless parameter Π/P (a) and corresponding emittance contours (b). The intensity of the argon beam is constant (2 mA); the variation of Π/P is obtained from the variation of the accel voltage. (c) Fractional normalised emittance enclosed within equidensity contours and emittance of the circumscribing ellipse as functions of Π/P . The equidensity contours are defined by the quoted percentage of the maximum density. 28

Parameters of High-Intensity LEBT

Location	Particle, Energy	Type	Beam current, mA	Rms beam emittance (π mm mrad)	Chopper
SNS	H ⁻ , 65 keV	2 Einzel lenses	35	0.22/0.18	40 kV Electrode chopper
J-Park	H ⁻ , 50 keV	2 Solenoids	35	0.22	Induction cavity
BNL	H ⁻ , 35 keV	2 Solenoids	100	0.4	
FNAL	H ⁻ , 35 keV	2 Solenoids	45	0.3	Einzel lens chopper
LANSCE	H ⁻ , 80 keV	2 solenoids	17	0.2	Electrostatic deflector
CERN Linac4	H ⁻ , 45 keV	2 solenoids	40	0.25	Electrostatic deflector
JHF 1996	H ⁻ , 50 keV	2 solenoids	16	0.1	
ISIS	H ⁻ , 65 keV	3 solenoids	60	0.55	
ESS	H ⁺ , 75 keV	2 solenoids	55	0.2	

Electrostatic LEBT

Pro:

- no transient time for space charge compensation
- no repelling electrode for the neutralizing particle trapping is needed- design of electrostatic LEBTs are simplified
- the beam lines are compact, which tends to minimize the beam losses by charge exchange

Con:

- no space charge compensation (neutralizing particles are attracted or re-pulsed by the electric field induced by the focusing elements).
- vulnerable to beam losses that can lead to high voltage breakdowns and beam trips
- Einzel lenses intrinsically induce optical aberrations that creates beam halo and emittance growth
- Electrostatic LEBTs are intensity limited. Beam divergence and size will increase rapidly with its intensity (especially for current of several tens of mA). Its seems difficult to operate the LEBT with a higher current than the design current without expecting beam losses or dramatic emittance growth.

SNS LEBT and parameters of the beam

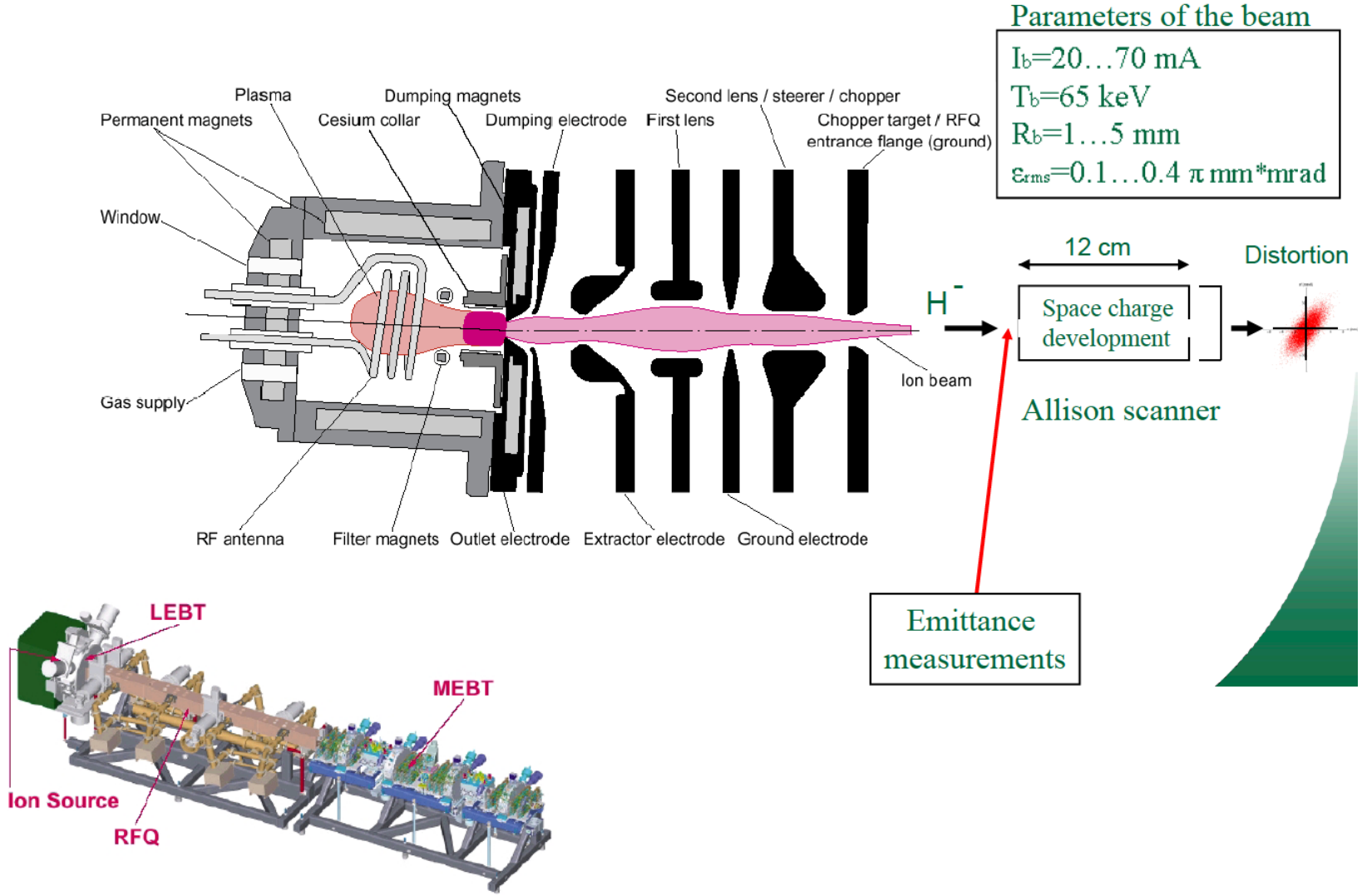


Figure 1. The 9-m long SNS front-end beamline.

SNS Injector Beam Parameters

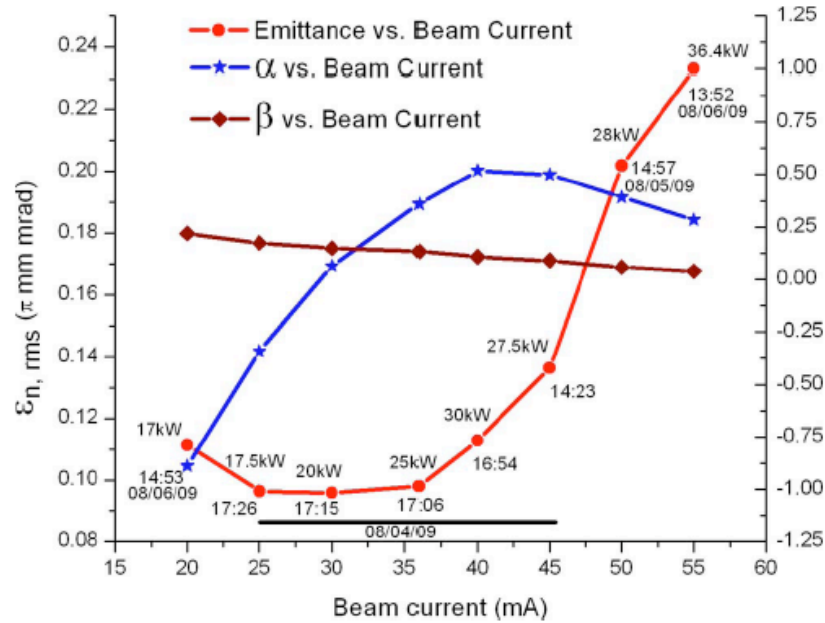


FIG. 5. (Color online) Emittance and twiss parameters dependence on the beam intensity.

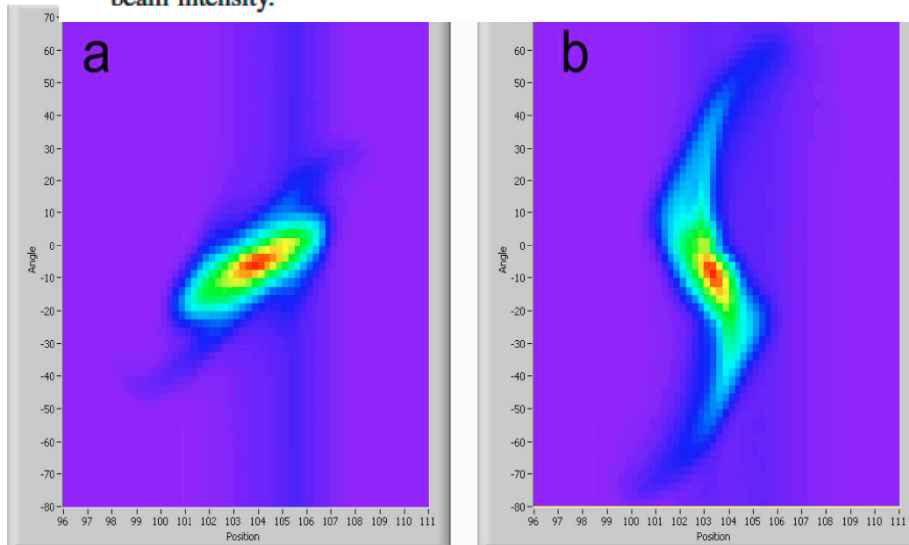


FIG. 6. (Color online) Phase-space plots of (a) 20 and (b) 55 mA beams.

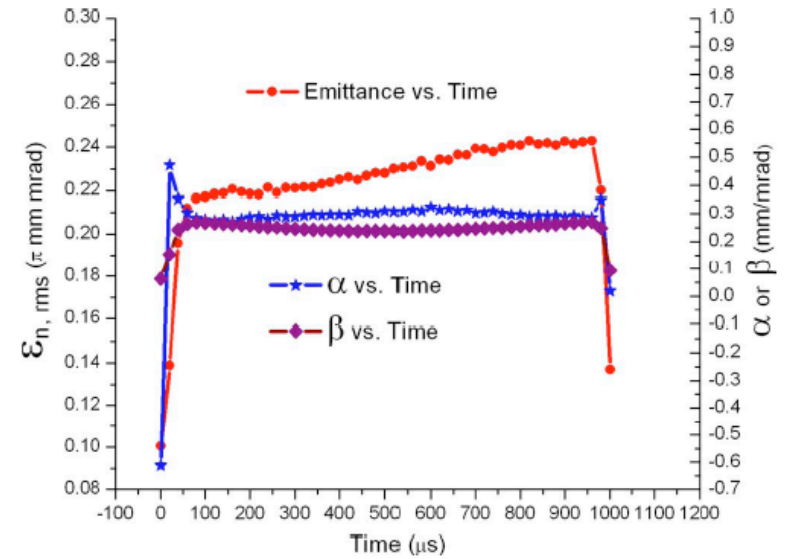


FIG. 8. (Color online) Evolution of the emittance and twiss parameters over the 1.0 ms beam pulse duration.

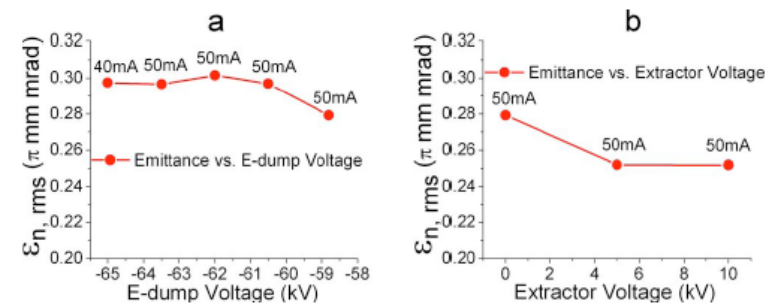


FIG. 7. (Color online) Emittance dependences on (a) e-dump voltage with the extractor at ground and (b) extractor voltage with the e-dump set at -58.8 kV.

Magnetostatic LEBT

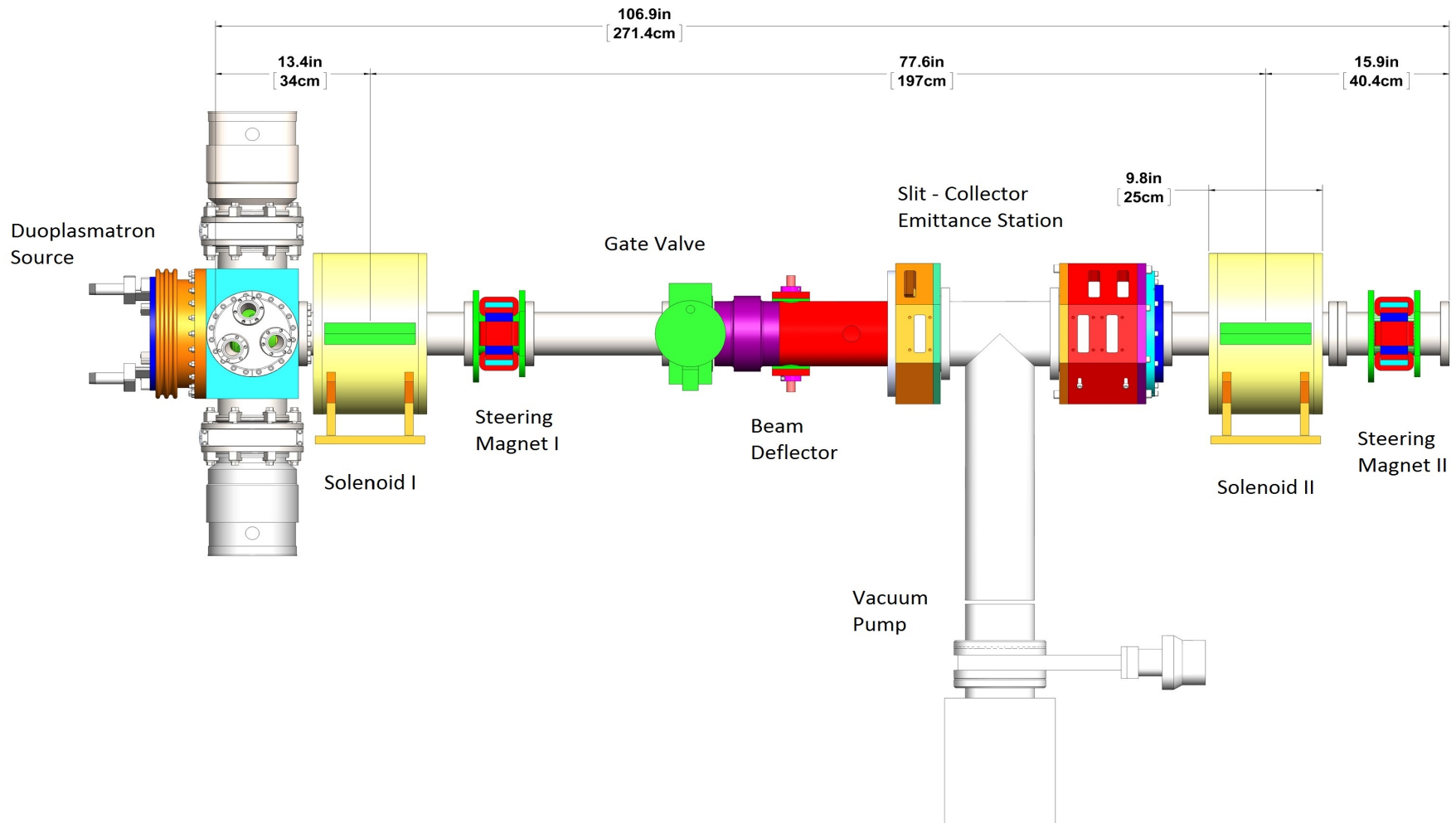
Pro:

- beam is neutralized by the ionization on the residual gas
- smaller emittance growth due to nonlinear space charge forces than that in electrostatic LEBT
- beam emittance can be improved with a higher pressure in the beam line
- for positive ion beam, an additional source of neutralizing particles exists: secondary electrons are produced when a beam hits the beam pipes
- magnetic lenses have less spherical aberrations than electrostatic lenses with the same focal length

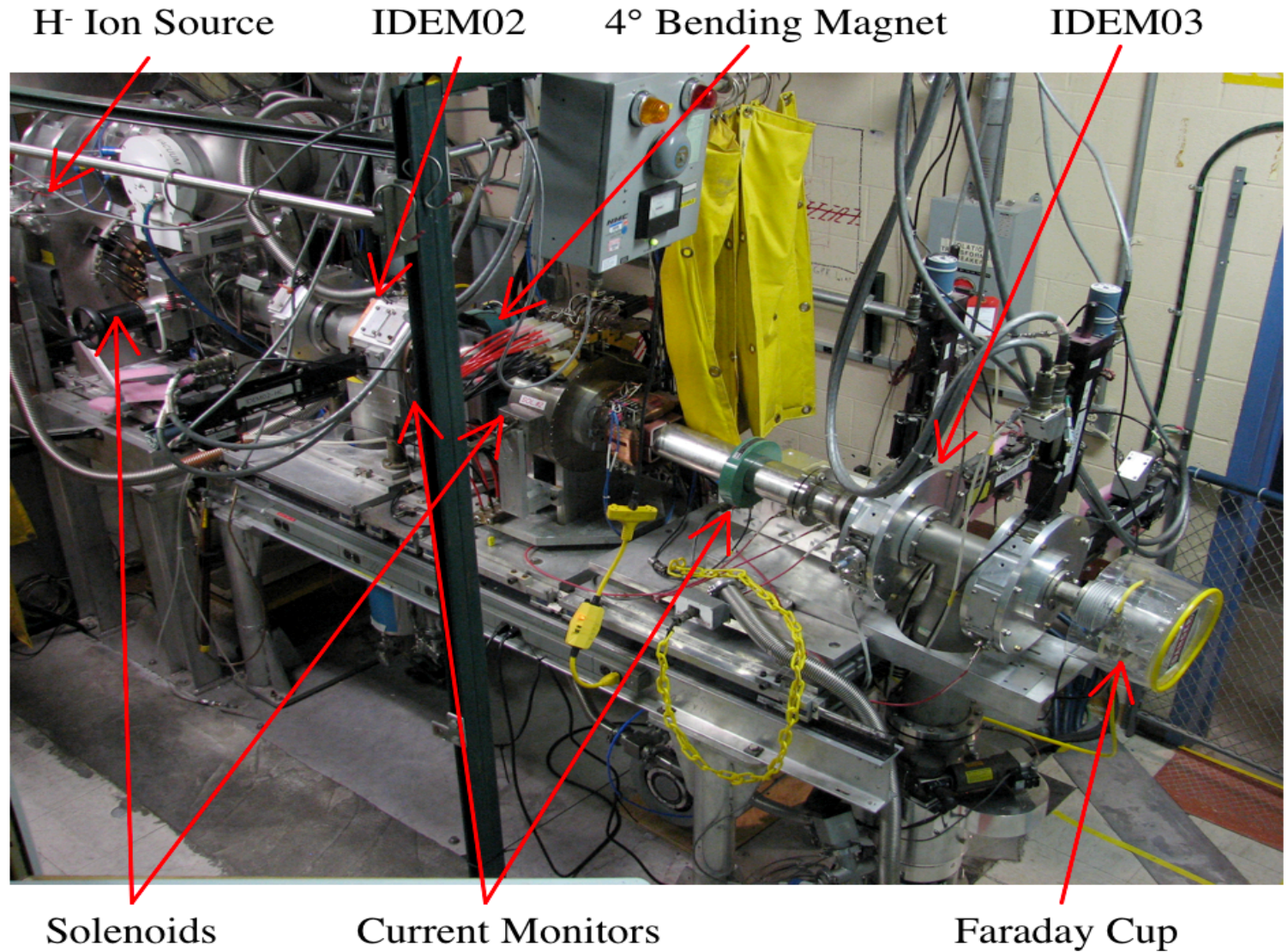
Con:

- In a magnetic LEBT the rise time of the pulsed beams is dominated by the space charge compensation transient time (several tens of μs)
- a fast chopping system have to be inserted to reach a rise time in the order of the hundreds of ns.

Layout of New LANSCE 35 keV H⁺ Injector

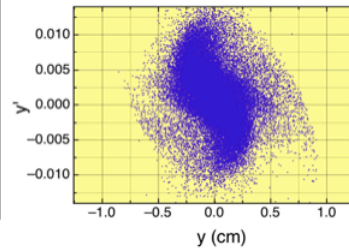
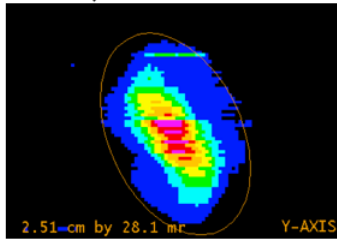


LANSCCE H⁻ 80 keV Low Energy Beam Transport

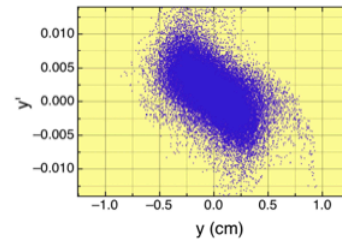
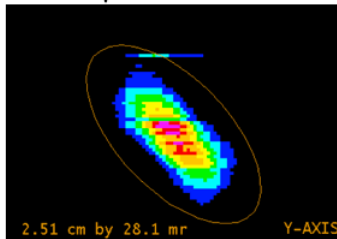


Effect of the Beam Space Charge Neutralization on Residual Gas

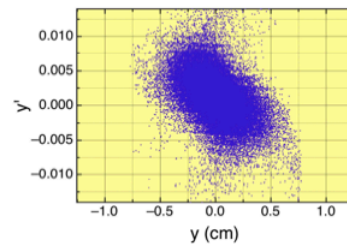
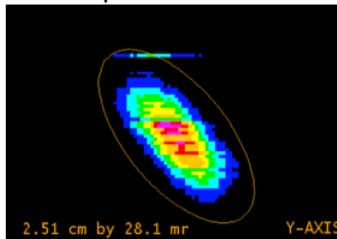
$\tau = 50 \mu\text{s}$



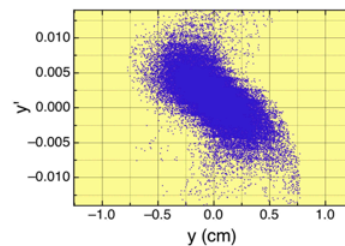
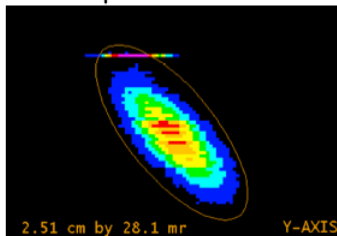
$\tau = 100 \mu\text{s}$



$\tau = 150 \mu\text{s}$

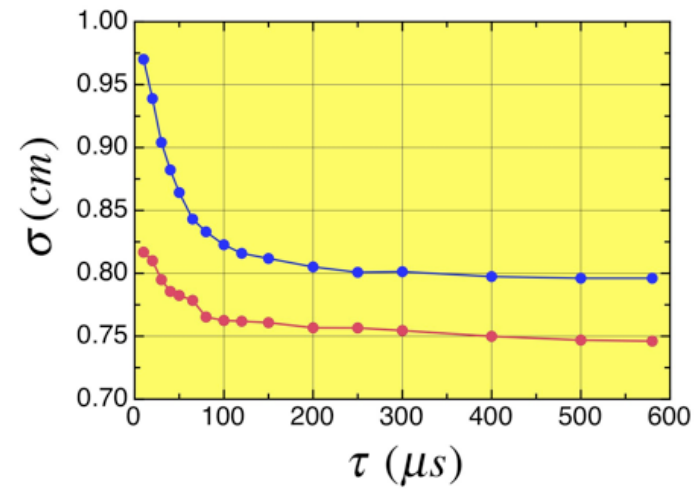
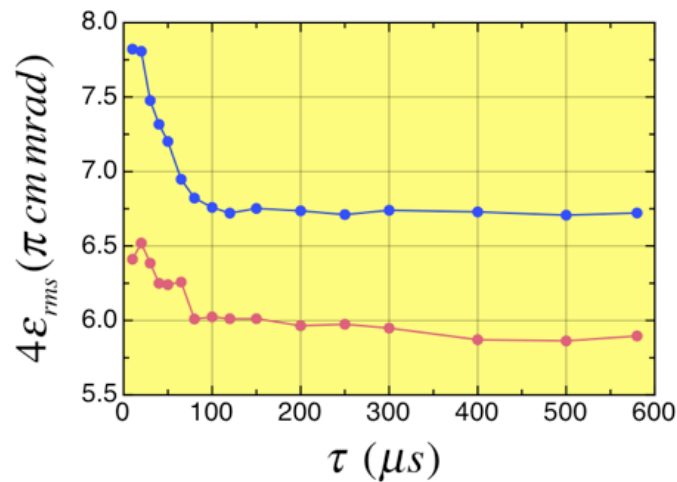
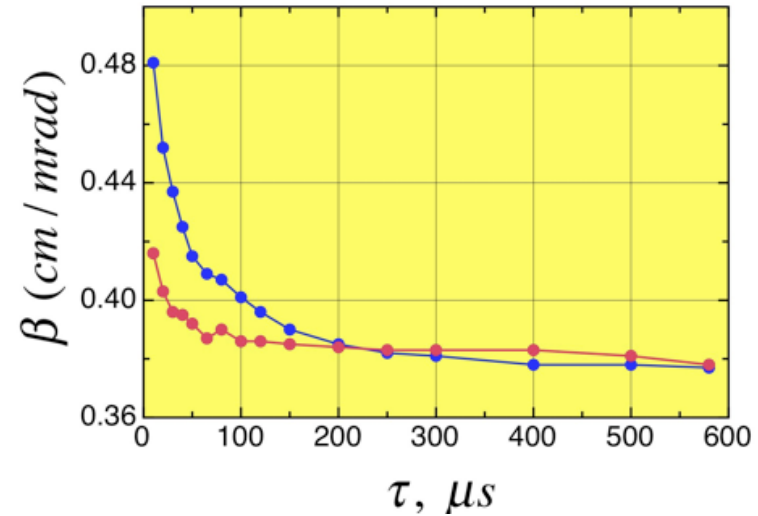
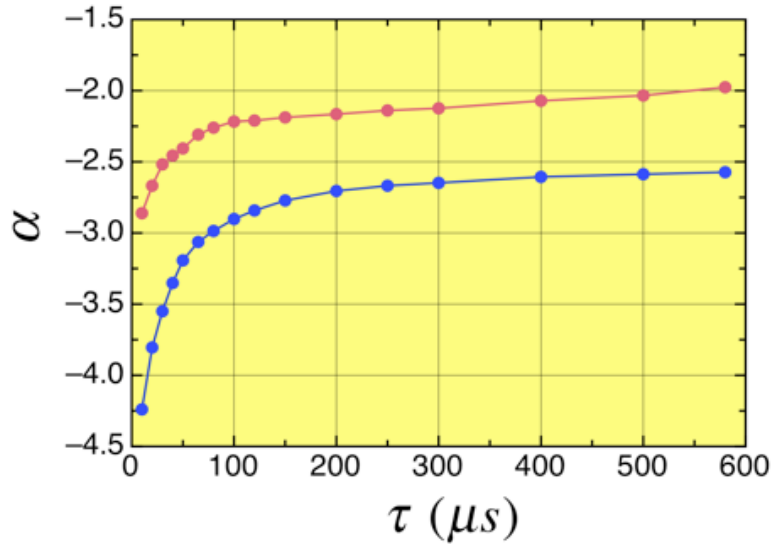


$\tau = 660 \mu\text{s}$



(Left)Measured vertical beam emittance at TBEM3 and (right) BEAMPATH simulations at different values of beam pulse length (simulations performed with current $I = 15 \text{ mA}$ for $t = 50\text{-}100 \text{ ms}$ and with current $I = 0$ for $\tau \geq 150 \mu\text{s}$.)

Effect of Space Charge Neutralization on Beam Parameters



Variation of 80 keV H- beam parameters during pulse length.

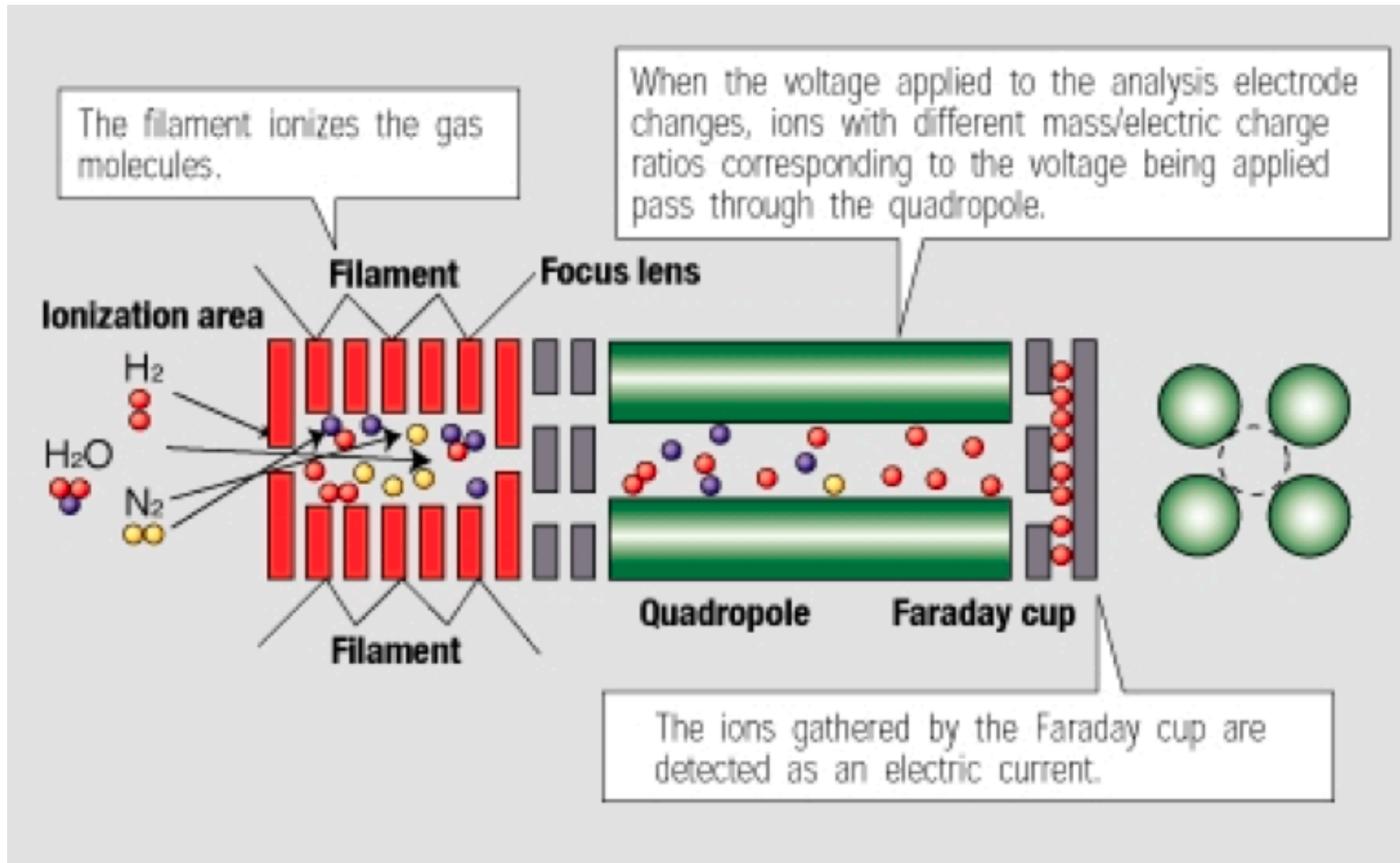
Low Pressure (Vacuum) Measuring Devices



Tubulated hot-cathode ionization gauge.

Electrons emitted from the filament move several times in back and forth movements around the grid before finally entering the grid. During these movements, some electrons collide with a gaseous molecule to form a pair of an ion and an electron. The number of these ions is proportional to the gaseous molecule density multiplied by the electron current emitted from the filament, and these ions pour into the collector to form an ion current. Since the gaseous molecule density is proportional to the pressure, the pressure is estimated by measuring the ion current.

Residual Gas Analyzer



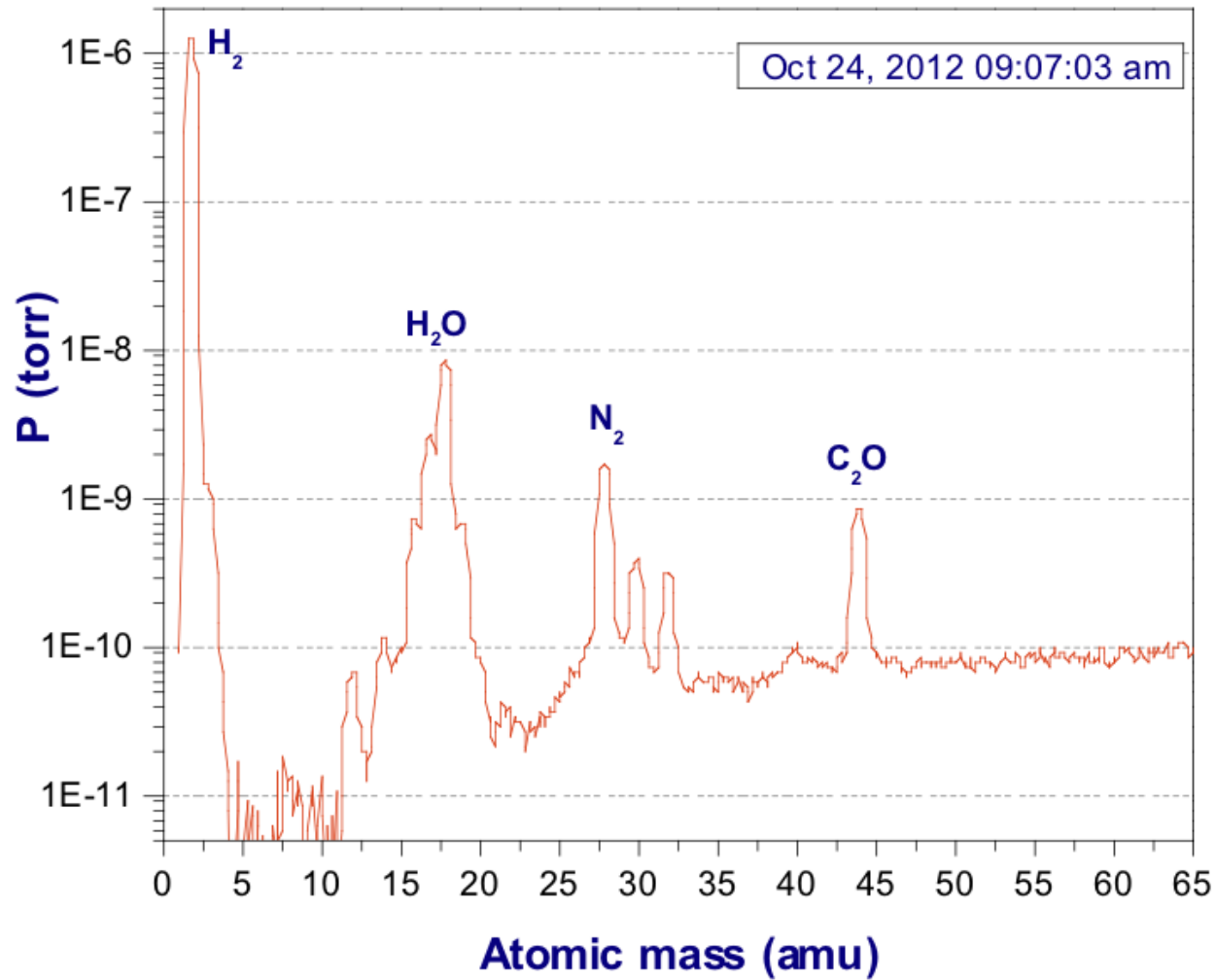
Pressure Units

Pressure units

V · T · E	Pascal	Bar	Technical atmosphere	Standard atmosphere	Torr	Pounds per square inch
	(Pa)	(bar)	(at)	(atm)	(Torr)	(psi)
1 Pa	$\equiv 1 \text{ N/m}^2$	10^{-5}	1.0197×10^{-5}	9.8692×10^{-6}	7.5006×10^{-3}	1.450377×10^{-4}
1 bar	10^5	$\equiv 10^6 \text{ dyn/cm}^2$	1.0197	0.98692	750.06	14.50377
1 at	0.980665×10^5	0.980665	$\equiv 1 \text{ kp/cm}^2$	0.9678411	735.5592	14.22334
1 atm	1.01325×10^5	1.01325	1.0332	$\equiv p_0$	$\equiv 760$	14.69595
1 Torr	133.3224	1.333224×10^{-3}	1.359551×10^{-3}	1.315789×10^{-3}	$\approx 1 \text{ mmHg}$	1.933678×10^{-2}
1 psi	6.8948×10^3	6.8948×10^{-2}	7.03069×10^{-2}	6.8046×10^{-2}	51.71493	$\equiv 1 \text{ lb}_f/\text{in}^2$

Residual Gas Spectrum

Analog Scan



Space Charge Neutralization Time

Time required for ionization of residual gas by the incoming beam with velocity of βc

n_s is the density of scattering gas centers, σ_i is the ionization cross section.

$$\tau_N = \frac{1}{n_s \sigma_i \beta c}$$

Number of molecules per unit volume at pressure p and temperature T determined from the ideal gas law:

$$n_g = \frac{p}{kT}$$

Boltzman constant

$$k = 1.38 \times 10^{-23} \text{ J}\cdot\text{K}^{-1}$$

Density of scattering centers for residual gas containing 2 atoms per molecule (H_2)

$$n_s = 2n_g$$

Ionization Cross Sections of H^+ on Different Gases

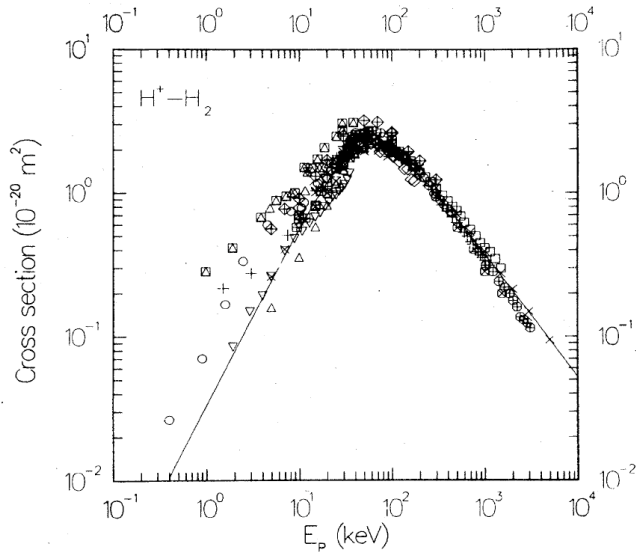


FIG. 13. Cross sections for ejection of electrons in $H^+ + H_2$ collisions. The solid curve is the recommended fit. Experimental data points are shown with various symbols.

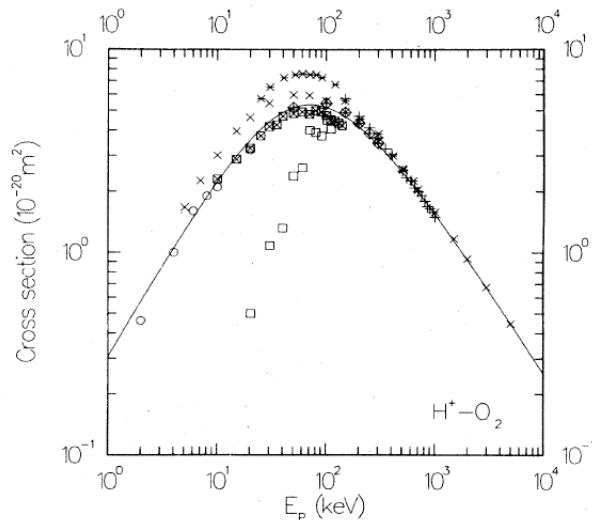


FIG. 16. Cross sections for ejection of electrons in $H^+ + O_2$ collisions. The solid curve is the recommended fit. Experimental data points are shown with various symbols.

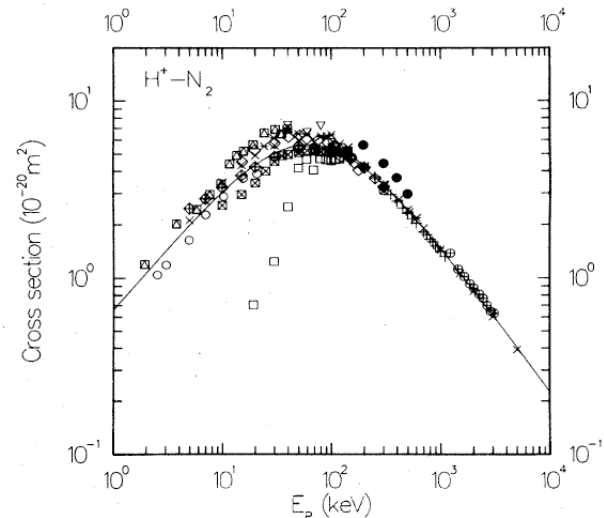


FIG. 14. Cross sections for ejection of electrons in $H^+ + N_2$ collisions. The solid curve is the recommended fit. Experimental data points are shown with various symbols.

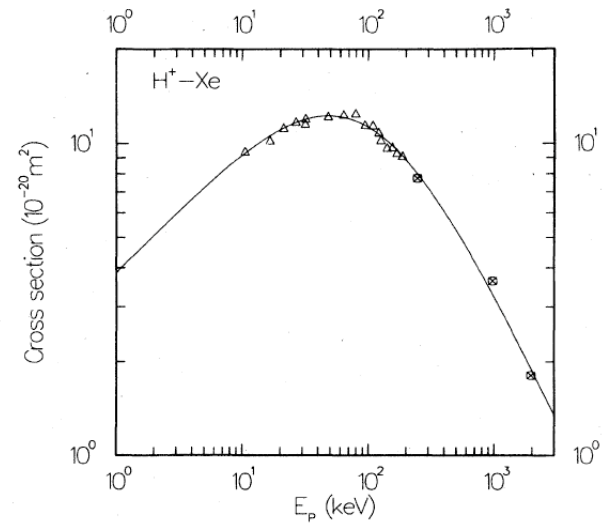
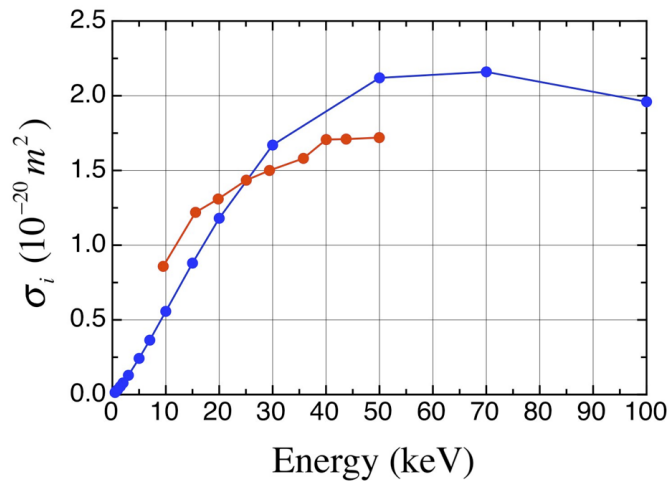


FIG. 11. Cross sections for ejection of electrons in $H^+ + Xe$ collisions. The solid curve is the recommended fit. Experimental data: Δ , Fedorenko *et al.* (1960); \boxtimes , Toburen (1974).

Space Charge Neutralization Time of 80 keV H⁻ Beam in H₂ Residual Gas with Pressure of P = 3.5 x 10⁻⁶ Torr



Density of H₂ molecules under the pressure of $p = 3.5 \cdot 10^{-6} \text{ Torr}$ ($4.6 \cdot 10^{-4} \text{ Pascal}$)

$$n_g = \frac{p}{kT} = 1.1 \cdot 10^{17} \frac{1}{m^3}$$

Ionization Cross Section for 80 keV

$$\sigma_i = 2.1 \cdot 10^{-20} m^2$$

Neutralization time

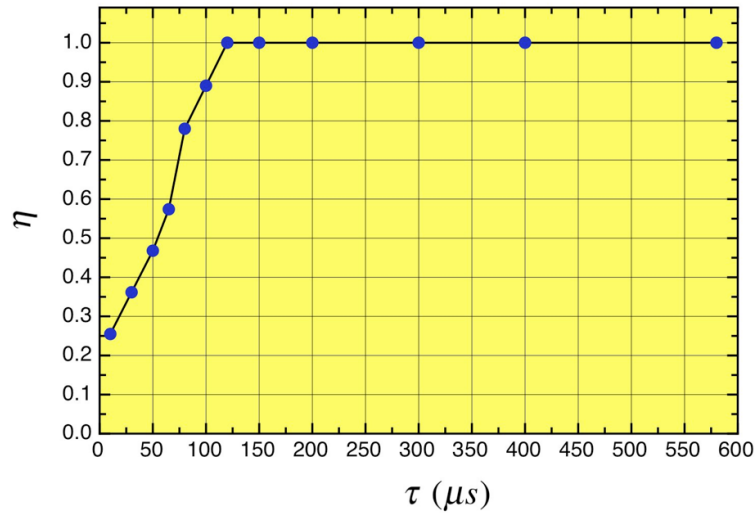
$$\tau_N = \frac{1}{2n_g \sigma_i \beta c} = 57 \mu s$$

Ionization cross-section of H₂ by H⁻ (red, Ref. [1]) and H⁺ (blue, Ref [2]) collisions.

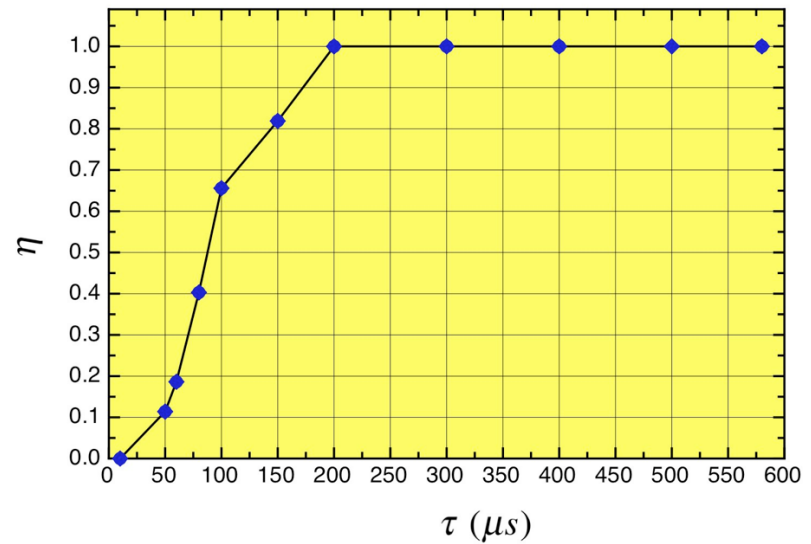
[1] Ya.M.Fogel, A.G.Koval, Y.Z.Levchenko, Zh. Eksp. Teor. Fiz., 38, 1053 (1960) [Sov. Phys. JETP 11, 760 (1960)].

[2] M.E.Rudd, Y.-K.Kim, D.H.Madison, J.W.Gallagher, Reviews of Modern Physics, 57, No.4, 965 (1985).

Measured Space Charge Neutralization of H- Beam within Pulse Length (H_2 Residual Gas with Pressure of $P = 3.5 \times 10^{-6}$ Torr)



Space charge neutralization of 80 keV H^- beam as a function of beam pulse length.



Space charge neutralization of 35 keV H^- beam as a function of beam pulse length.

Neutralization Time (μs) for 35 keV H^+ Beam in Different Gases

Gas	Ionization Cross Section (10^{-20} m^2)	10^{-5} Torr
H_2	1.67	36
He	0.494	243
Ne	1.09	110.3
N_2	5.0	11.9
O_2	4.41	13.6
Ar	5.11	23.5
Kr	7.24	16.6
Xe	11.9	10.1
CO	5.78	20.8

$$\tau_n = \frac{1}{\sigma_i n_{gas} v}$$

Improvement of 66 mA 95 keV H⁺ SILHI Source Beam Emittance by Heavy Gas Injection in LEBT (Rev. Sci. Instr., 71, 3, p. 1413, 2000)

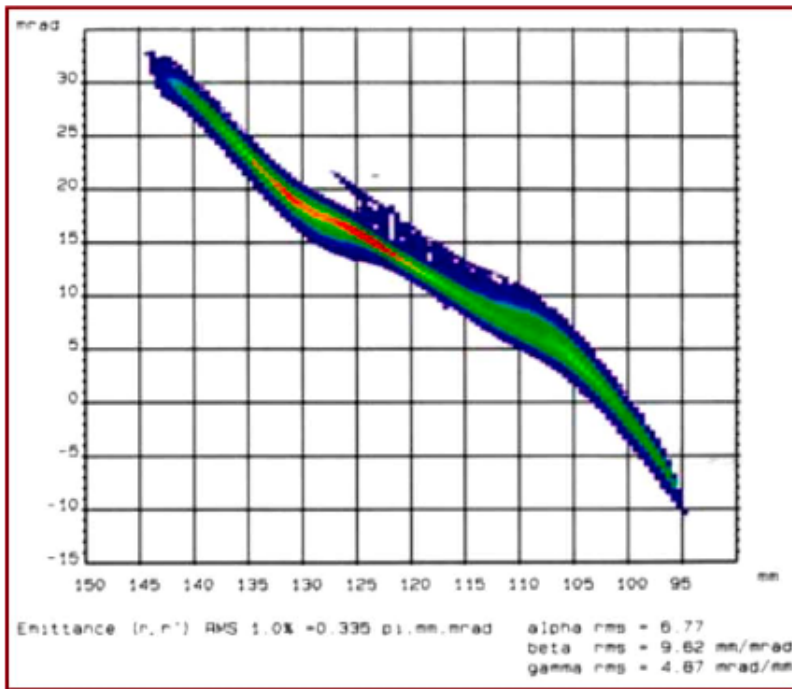


FIG. 2. ϵ rms norm=0.33 π mm mrad for a 66 mA 95 keV H⁺ beam ($P_{\text{real}}=4.3 \times 10^{-5}$ Torr).

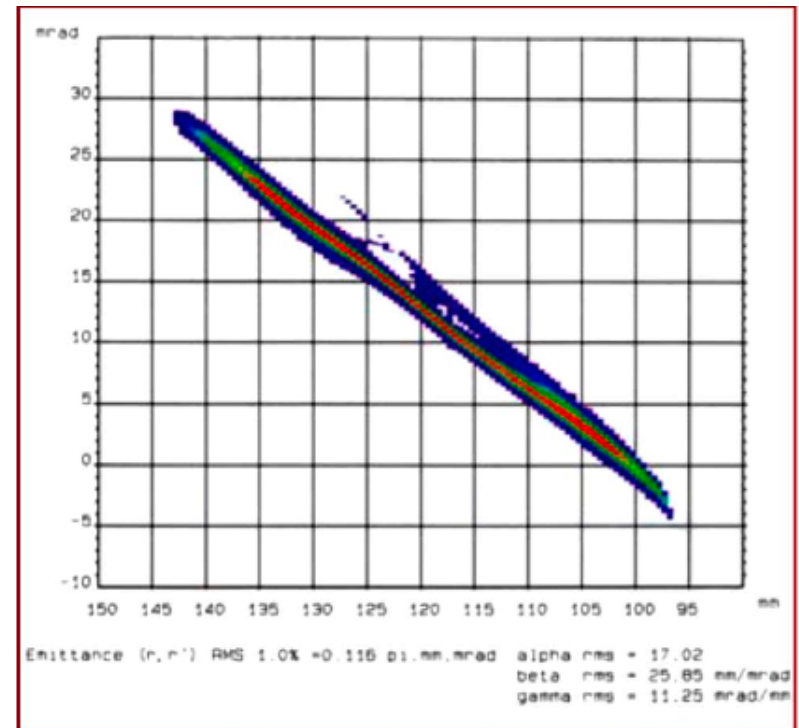
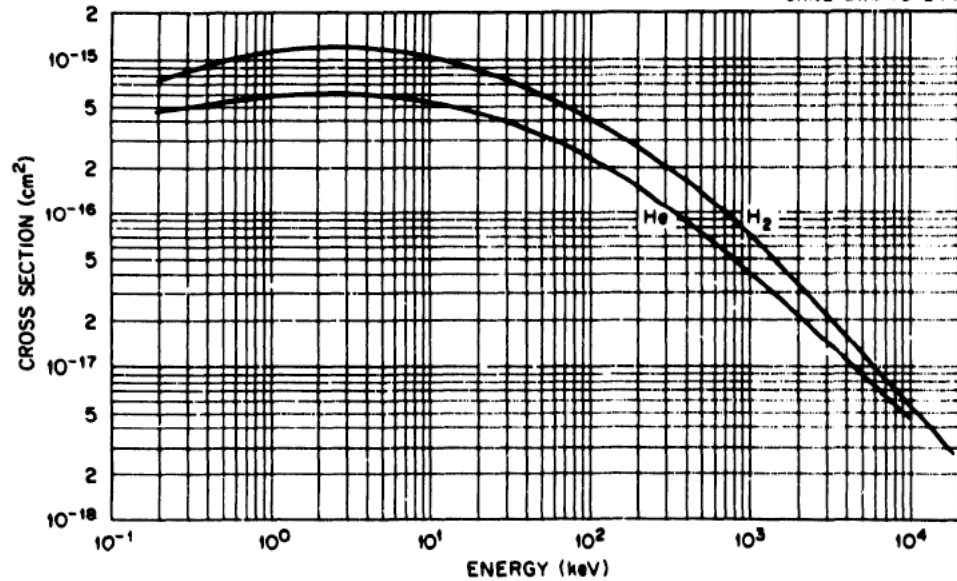


FIG. 3. ϵ rms norm=0.11 π mm mrad (r, r') for a 66 mA 95 keV H⁺ beam with Kr injection ($P_{\text{real}}=5.2 \times 10^{-5}$ Torr).

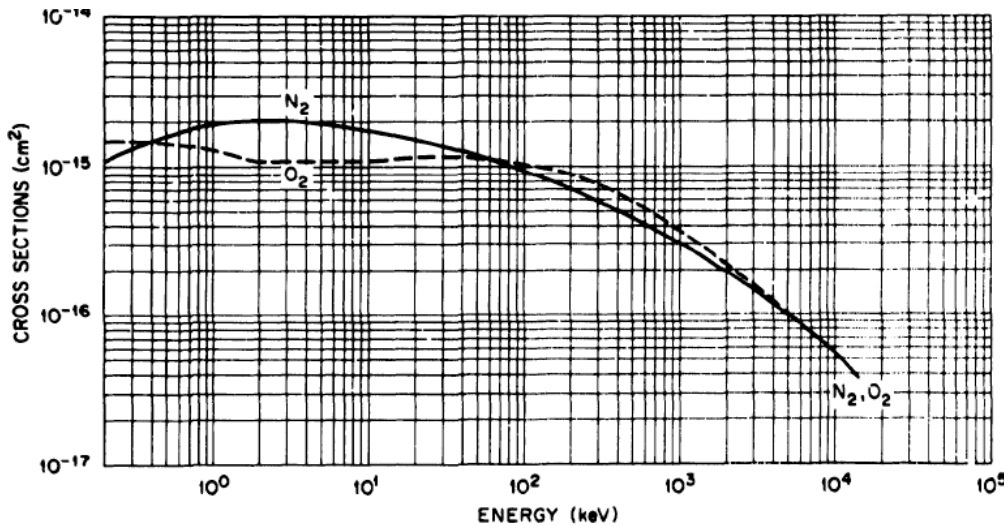
Cross Section for Stripping H⁻ in Different Gases (Atomic Data for Controlled Fusion Research, ORNL-5206)

ORNL-DWG 75-244

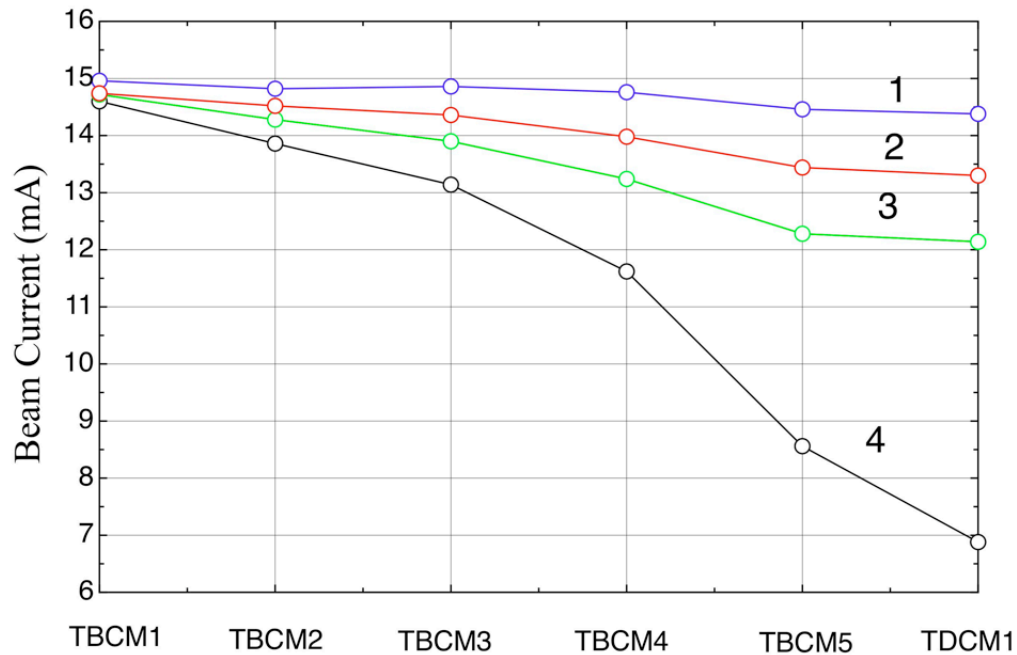


Single stripping cross-section σ_{-10}
of 750 keV H⁻ in different gases

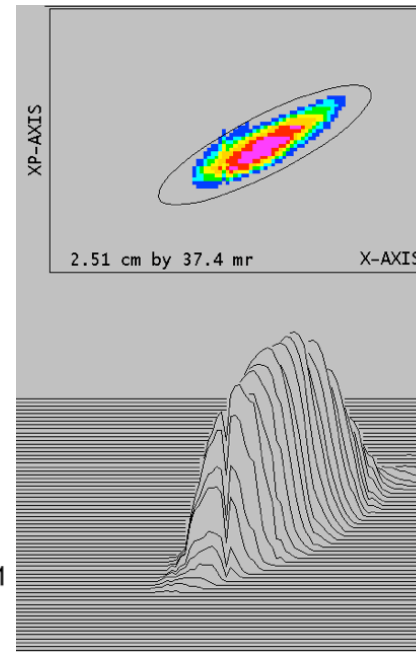
Gas	Cross section, cm ²
H ₂	$7 \cdot 10^{-17}$
He	$5 \cdot 10^{-17}$
N ₂	$3 \cdot 10^{-16}$
O ₂	$4 \cdot 10^{-16}$



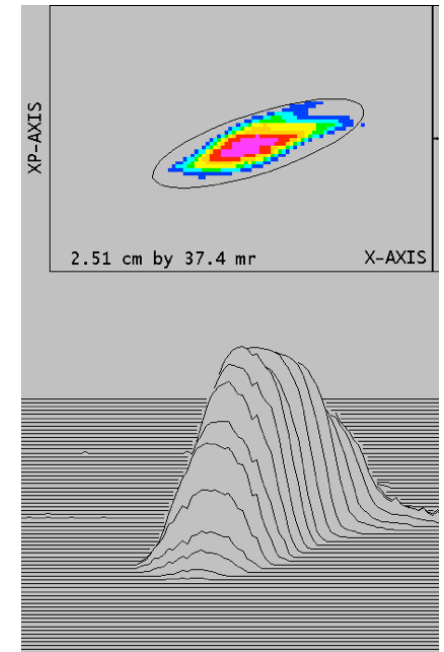
750 keV H- Beam Performance Under Different Vacuum Conditions



$7 \cdot 10^{-7}$ Torr



$3 \cdot 10^{-5}$ Torr

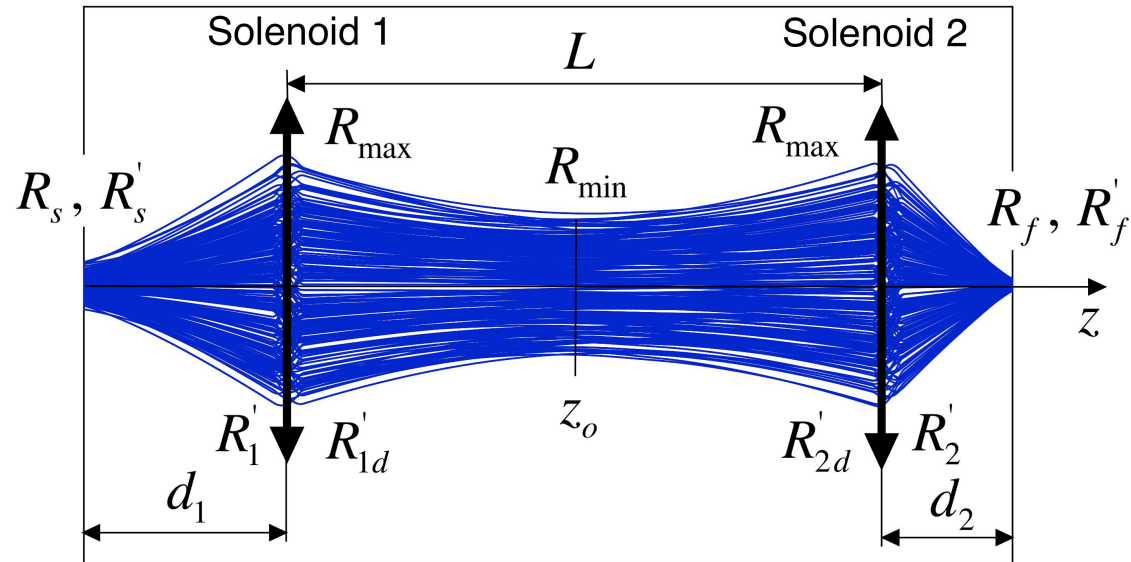


Beam transmission through LEPT as a function of vacuum conditions:

- (1) $4.6 \cdot 10^{-7}$ Torr,
- (2) $7.4 \cdot 10^{-6}$ Torr,
- (3) $1.3 \cdot 10^{-5}$ Torr,
- (4) $4.9 \cdot 10^{-5}$ Torr.

TDEM1 emittance scan with (left) nominal vacuum of $7 \cdot 10^{-7}$ Torr and (right) with vacuum of $3 \cdot 10^{-5}$ Torr.

Design of Magnetostatic LEBT



Initial Data:

Beam Current	I_o
Space charge neutralization factor	η
Effective beam current	$I = I_o(1 - \eta)$
Unnormalized beam emittance	\mathfrak{E}
Initial envelope parameters	R_s, R'_s
Final envelope parameters	R_f, R'_f
Distance between solenoids	L

To Be Determined:

- Solenoid Geometry and Fields
- Distances d_1, d_2

Minimization of Beam Size in LEBT

Consider beam with negligible current, but with finite value of beam emittance (emittance-dominated beam). Evolution of beam radius R along drift space z between solenoids as a function of initial radius R_o and slope of the envelope R_o' is given by integration of envelope equation assuming $I = 0$:

$$\frac{R}{R_o} = \sqrt{\left(1 + \frac{R_o'}{R_o} z\right)^2 + \left(\frac{\mathfrak{A}}{R_o^2}\right)^2 z^2} \quad (5.1)$$

From the symmetry point of view it is clear, that matched beam has a minimum size, or waist, $R_{min} = R_o$ in the middle point of the drift space between lenses, and maximum size R_{max} inside focusing elements. At the waist point, $R_o' = 0$. Therefore from Eq. (5.1)

$$R_{max}^2 = R_{min}^2 + \left(\frac{\mathfrak{A}L}{2R_{min}}\right)^2 \quad (5.2)$$

Equation $\partial R_{max} / \partial R_{min} = 0$ determines minimal value of R_{max} as a function of beam emittance and distance between lenses

$$\frac{\partial R_{max}}{\partial R_{min}} = \frac{1}{\sqrt{R_{min}^2 + \left(\frac{\mathfrak{A}L}{2R_{min}}\right)^2}} \left[R_{min} - \frac{1}{R_{min}^3} \left(\frac{\mathfrak{A}L}{2}\right)^2 \right] = 0 \quad (5.3)$$

Solution of Eq. (5.3) is

$$R_{min}(0) = \sqrt{\frac{\mathfrak{A}L}{2}} \quad R_{max}(0) = \sqrt{\mathfrak{A}L} \quad (5.4)$$

which coincides with periodic solution of matched beam with zero current at phase advance of $\mu_o \approx \pi/2$. Eq. (5.4) determines the minimum value of R_{max} at given value of beam emittance and given distance between solenoids L .

Consider now space-charge dominated regime, where beam emittance is negligible. Analysis of beam dynamics in drift space determines the condition for transporting beam with maximum current through drift space restricted by aperture R_{max} and distance L :

$$R_{max} = \frac{L}{1.082} \sqrt{\frac{I}{I_c (\beta\gamma)^3}}, \quad R_{min} = \frac{R_{max}}{2.35} \quad (5.5)$$

In more general case, when both beam emittance and beam current are not negligible, precise value of R_{max} is determined by variation of the value of R_{min} at the middle point between solenoids, $z = z_o$, and searching for the smallest value of the beam size at the center of solenoids R_{max} via an exact solution of the envelope equation in drift space between solenoids.

Determination of Lens Parameters and Distances d_1, d_2

After determination of the minimal value of R_{max} , the distances d_1, d_2 are defined by integration of envelope equation in drift space to establish points where the beam radius evolves from initial value of R_o to R_{max} :

$$z = \frac{R_o^2}{2\vartheta} \int_1^{\left(\frac{R_{max}}{R_o}\right)^2} \frac{ds}{\sqrt{\left[1 + \left(\frac{R_o R_o'}{\vartheta}\right)^2\right]s + \left(\frac{PR_o}{\vartheta}\right)^2 s \ln s - 1}} . \quad (5.7)$$

In Eq. (5.7), the values of R_o, R_o' correspond to either R_s, R_s' or R_f, R_f' . Slopes of beam envelopes at solenoids R_1', R_2' can be found from the first integral of envelope equation in drift space:

$$R' = \sqrt{\left(R_o'\right)^2 + \left(\frac{\vartheta}{R_o}\right)^2 \left[1 - \left(\frac{R_o}{R}\right)^2\right] + \frac{2I}{I_c(\beta\gamma)^3} \ln\left(\frac{R}{R_o}\right)^2} . \quad (5.8)$$

The values of R_{1d}', R_{2d}' are determined by the first integral assuming $R_o = R_{min}, R_o' = 0$. Then, focal lengths of solenoids f_1, f_2 , are determined by the total change in the slope of the beam at each solenoid:

$$f_1 = \frac{R_{max}}{\left|R_{1d}'\right| + \left|R_1'\right|}, \quad f_2 = \frac{R_{max}}{\left|R_{2d}'\right| + \left|R_2'\right|} . \quad (5.9)$$

After that, the magnetic field within each solenoid is determined from thin lens approximation as

$$B_o = \frac{2mc\beta\gamma}{q\sqrt{fD}} . \quad (5.10)$$

Minimization of Emittance Growth in Lens due to Spherical Aberrations

The emittance growth due to spherical aberrations is estimated as:

$$\frac{\vartheta}{\vartheta_o} = \sqrt{1 + K \left(\frac{C_\alpha R^4}{f \vartheta_o} \right)^2} \quad (23)$$

where the coefficient $K = 0.05 \dots 0.5$ depends on the beam distribution. Let us restrict the emittance growth due to spherical aberrations to a value of 10%. Assuming that the beam has a waterbag distribution ($K = 0.114$), the following combination of parameters is restricted to be

$$\frac{C_\alpha R^4}{f \vartheta_o} < 1.35. \quad (24)$$

The value of the spherical aberration coefficient c_α can be expressed as a function of the pole piece aperture a and pole gap width S as

$$C_\alpha = \frac{5}{(S + 2a)^2}. \quad (20)$$

The field distribution within a solenoid is well approximated as

$$B(z) = \frac{B_o}{1 + \left(\frac{z}{d}\right)^4} \quad (21)$$

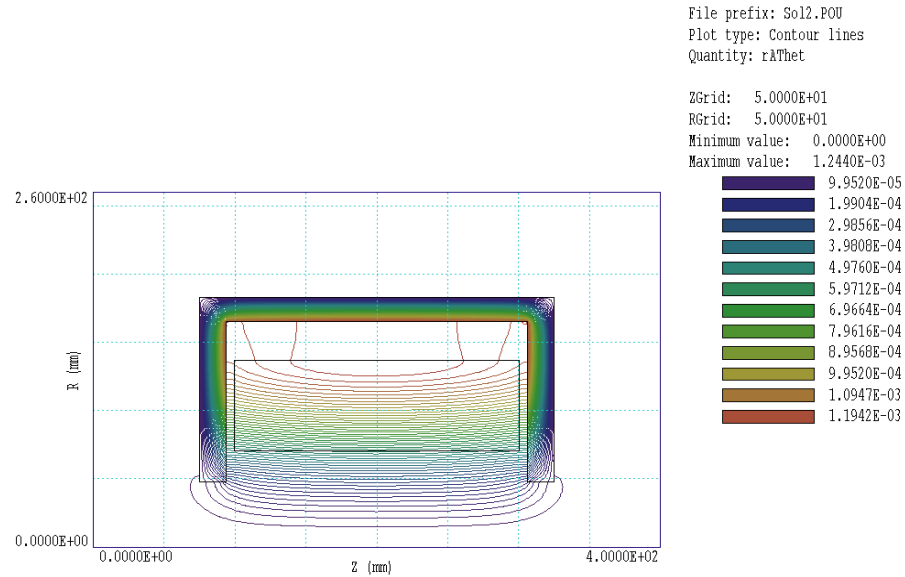
where B_o is the maximum field in solenoid, and d is the field profile characteristic length. The effective solenoid length, D , and spherical aberration coefficient C_α can be expressed in terms of a characteristic parameter d as

$$D = \frac{3\pi}{4\sqrt{2}} d, \quad C_\alpha = \frac{5}{12d^2}. \quad (22)$$

Then, from Eq. (22), the characteristic length of field distribution, d , has to be larger than

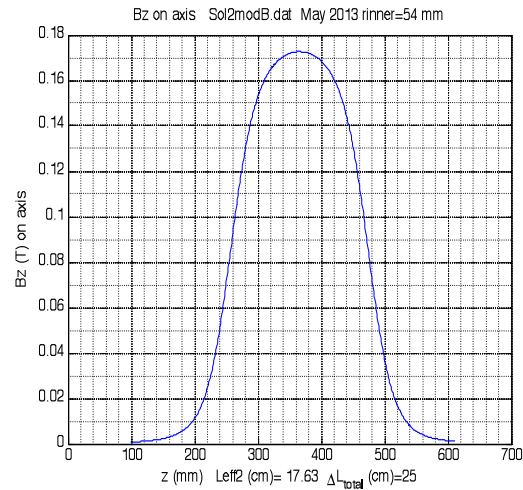
$$d > \sqrt{\frac{5}{12C_\alpha}} \quad (25)$$

Example of Solenoid Design



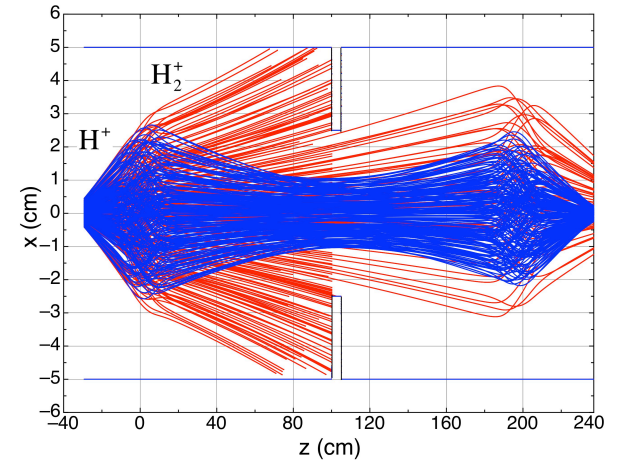
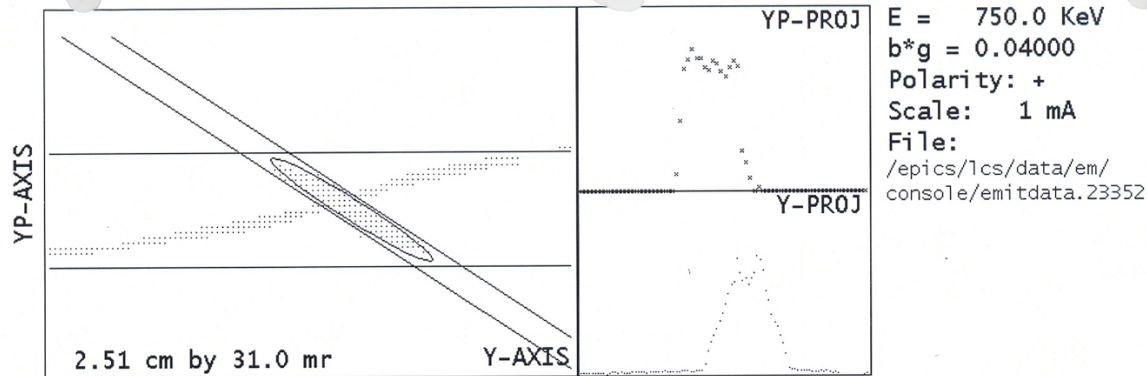
Physical length
 Effective length D
 Aperture radius
 Coil current density
 Maximum current density required for cooling

25 cm,
 17.63 cm,
 5.4 cm,
 3.1 Amps/mm²
 10 Amps/mm²

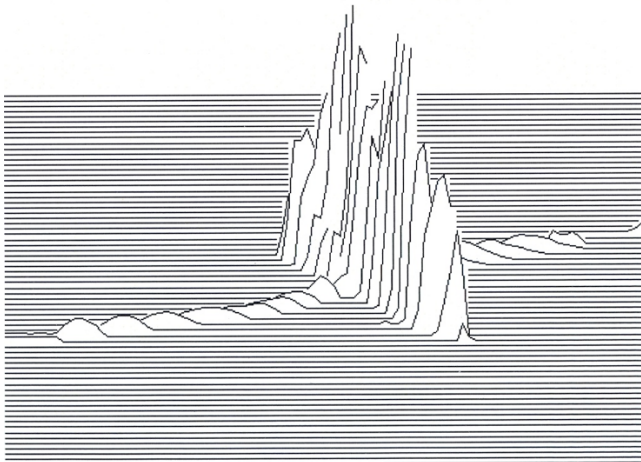


Solenoid and axial field distribution.

Separation of Beam Components in LEBT



Dynamics of 2- component beam in LEBT with collimator

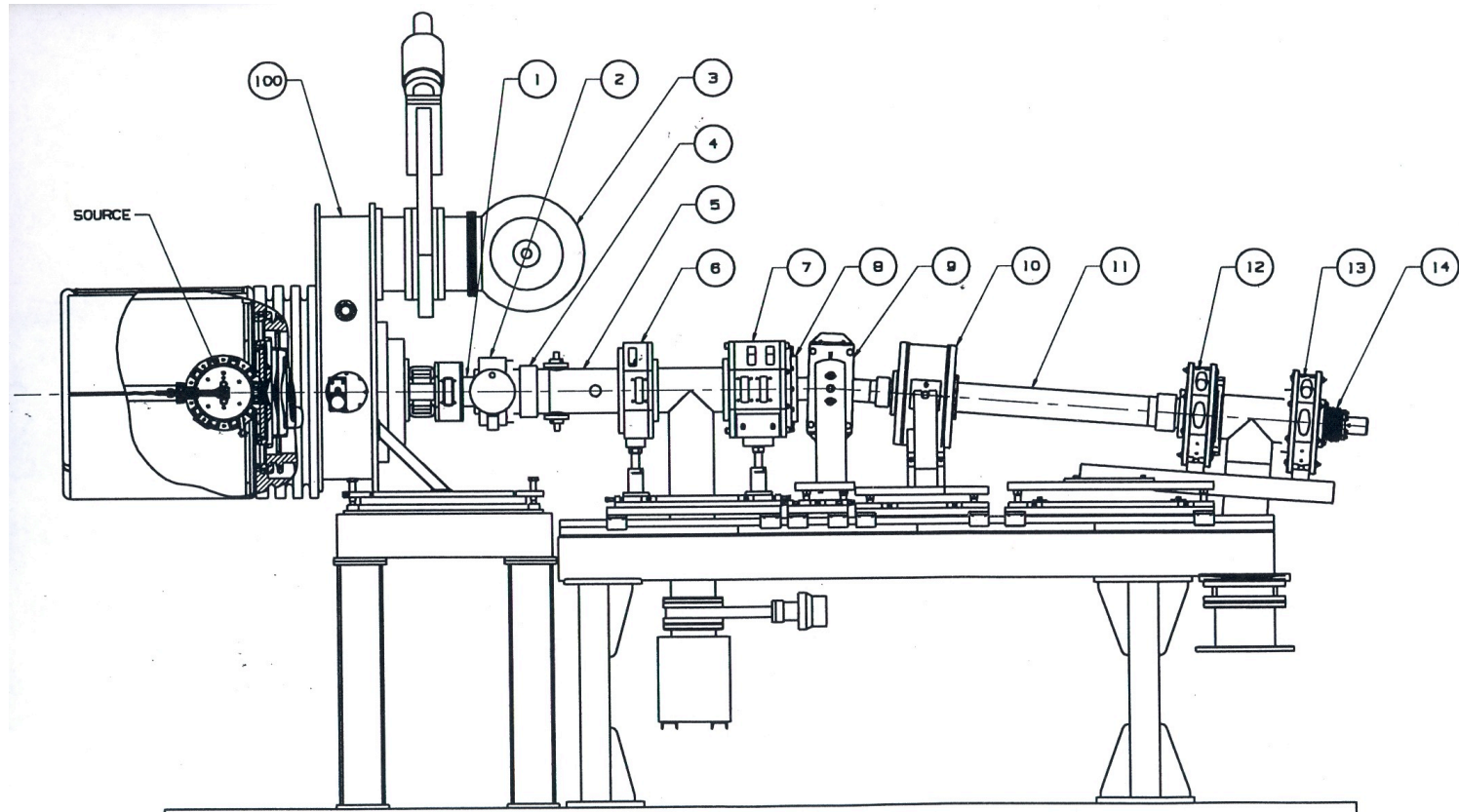


```

Run:23352      Stn: TAEM01-V
01:36:28      01-Mar-2012
Beam: H+       Meas, Norm
E(total) =    0.415, 0.017 pi
E(edge) =    0.346 pi
E(rms) =    0.073, 0.003 pi
Etot/rms =    5.72
Alpha =    4.124
Beta =    0.369
4*E(rms) =    0.290 pi
C =    0.202 cm
CP =    -1.413 mr
X Sigma =    0.1636 cm
XP Sigma =    1.8811 mr
Thold =    2.0 %, 25 cnts
Maximum Counts =    1292
Beam thru thresh =    52761
Total Beam =    52892
Clctr Pos =    1339 1878
Jaw Pos =    1293 1851
    
```

Measured H⁺ transverse phase space at 750 keV for the LANSCE duoplasmatron source. H₂⁺ beam is also observed. Beam current is 15.9 mA. Ratio of $\epsilon_{total} / \epsilon_{rms} = 5.7$. Straight lines are used to restrict phase space area where beam emittance is determined.

Bending Magnet



The separation angle between two beam components after a dipole bending magnet with bending angle, a , is given by:

$$\Delta\alpha = \alpha \left(1 - \frac{q_1 p_2}{q_2 p_1} \right)$$

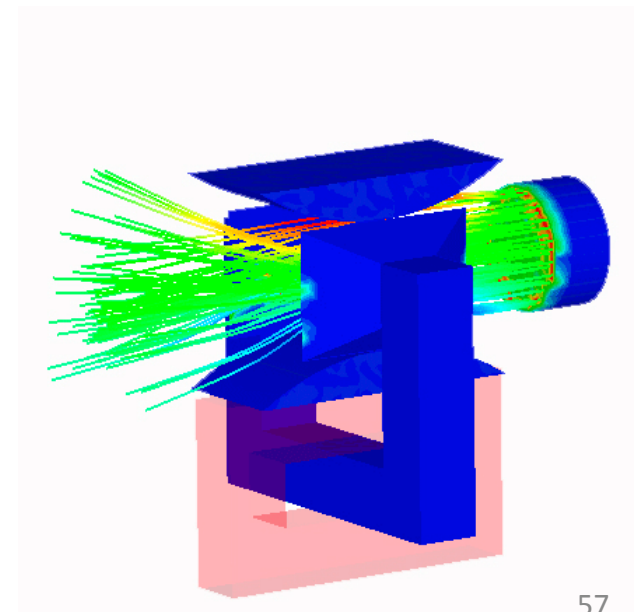
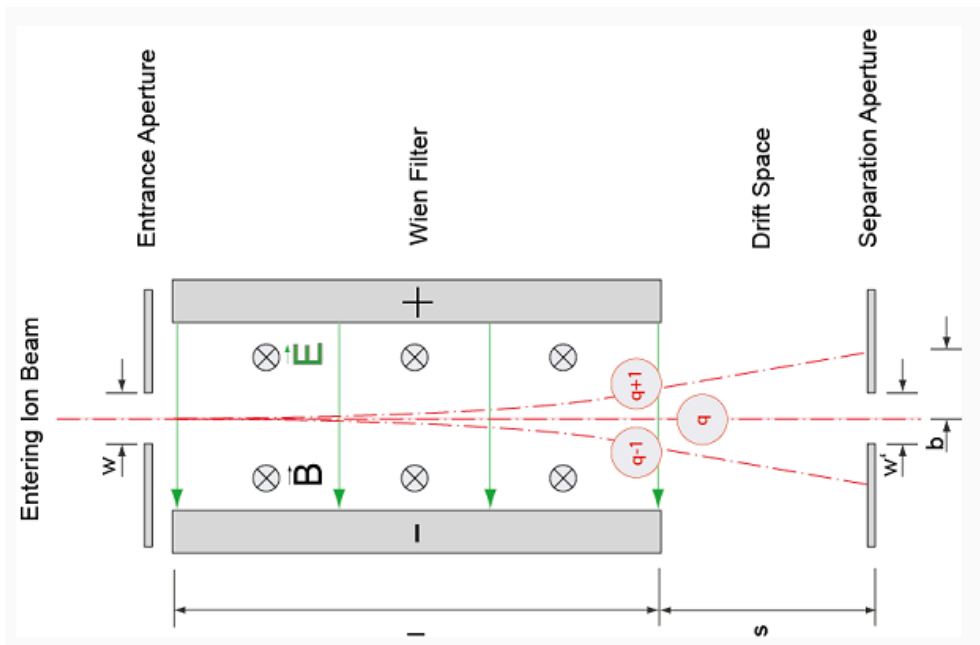
Wien Filter

In a Wien filter, a crossing $E \times B$ field is used to separate the beams. The primary beam is not deflected because of the balance between the electric and magnetic Lorentz force:

$$\int \vec{F}_{defl} dz = q \int (\vec{E} + \vec{v} \times \vec{B}) dz = 0 \quad (32)$$

The fields in the Wien filter are selected to cancel out for the primary, desired beam but act as a filter for other beam components, where the conditions of Eq. (32) are not met. The separation angle between 2 components after a Wien filter with field $E_{Wien} = \beta_1 c B_{Wien}$ is

$$\Delta\alpha = \frac{E_{Wien} L_{Wien} q_2}{m_2 \gamma_2 (\beta_2 c)^2} \left(1 - \frac{\beta_1}{\beta_2}\right) \quad (33)$$



Mismatch Effect in Wien Filter

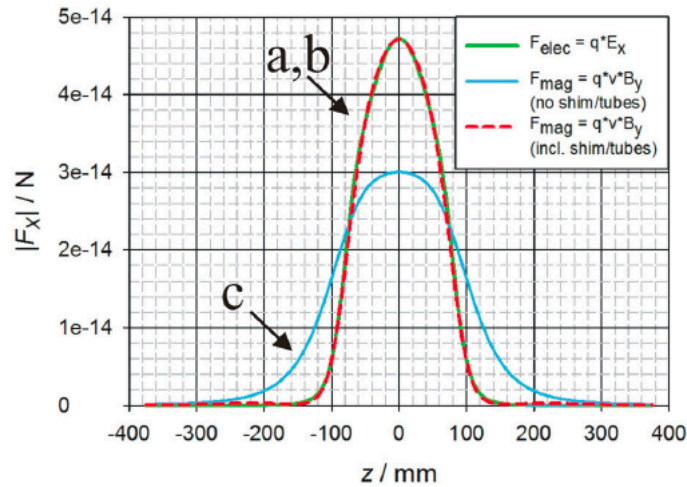


Figure 4: Calculated deflecting forces for on-axis particles (Curve a,b: matched case, c: without shimming).

The beam can pass the chopper without deflection, if the Wien condition is satisfied along the system:

$$\int \vec{F}_{defl} dz = \int q \cdot (\vec{E} + \vec{v}_p \times \vec{B}) dz = 0 \quad (1)$$

But a local mismatch between both fields can still lead to a transverse offset. This effect will be minimized by installing shims and shorting tubes at the dipole while the electric deflector will utilize curved plates and shims. The calculated deflecting forces for on-axis particles travelling in longitudinal direction are presented in Fig. 4. Electric and magnetic fields were computed using CST EMS [6].

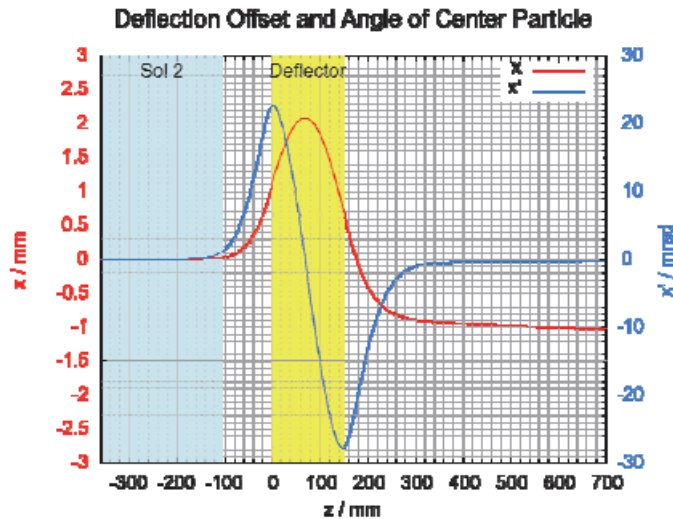


Figure 2: Horizontal movement of the center particle along the chopper axis z for the locally mismatched case.

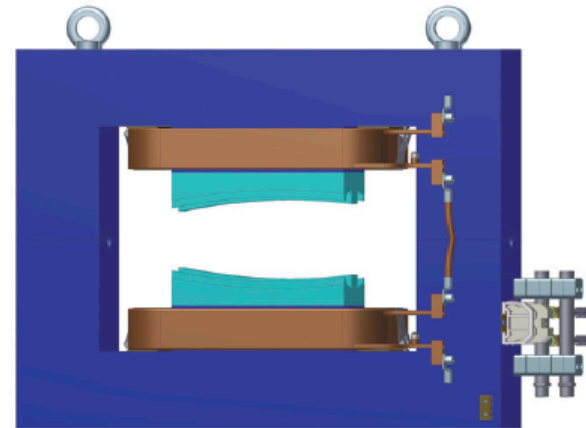
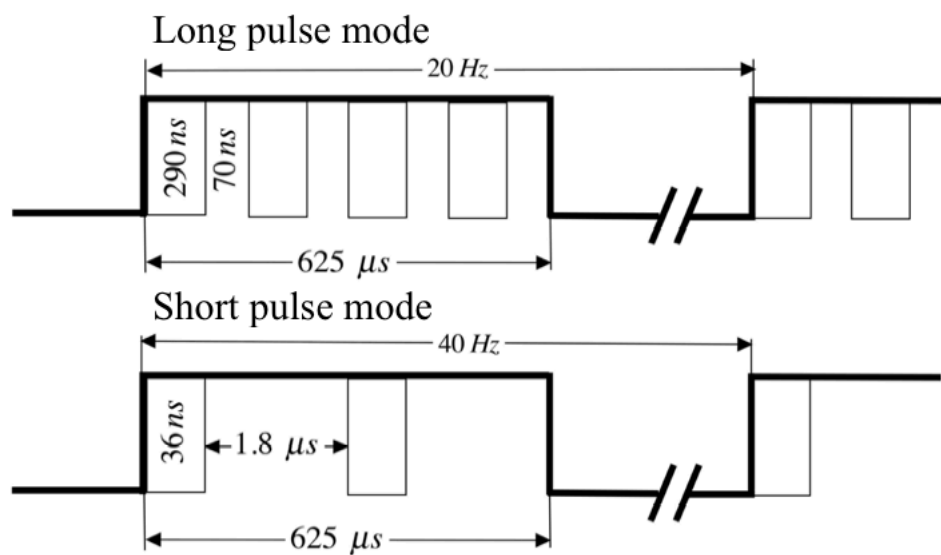
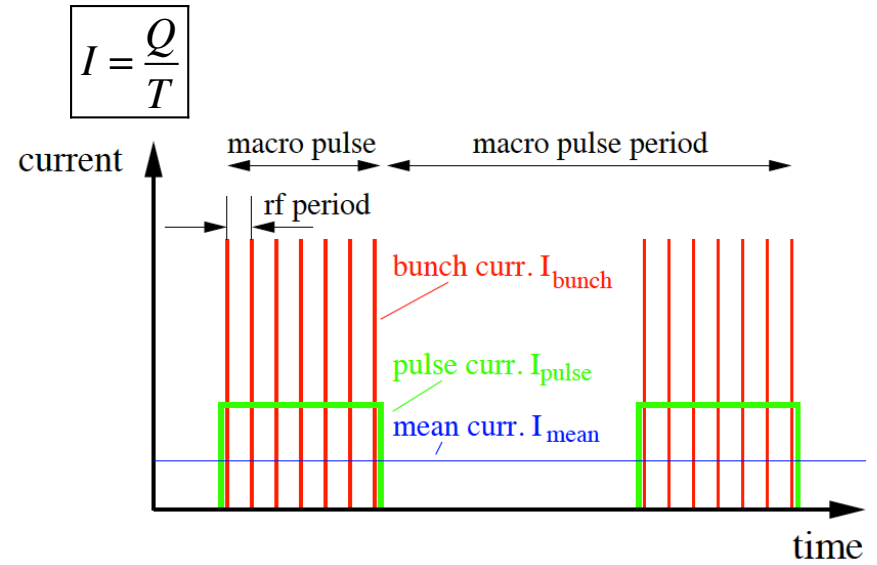


Figure 7: Drawing of chopper dipole with tilted and curved poles.

Beam Chopping



Pulse structure of LANSCE beam

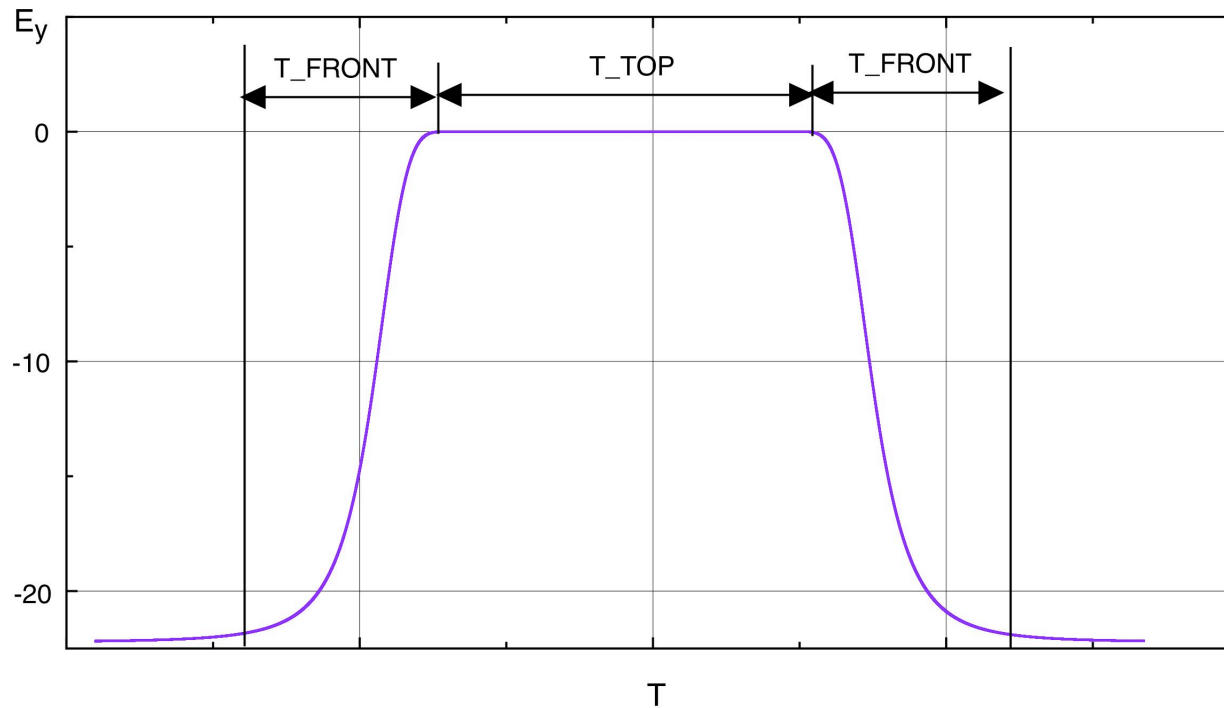


Time structure of different currents in LINAC (P.Forck, 2011)



LANSCE slow wave transmission line chopper

Chopper pulse



Short pulse beam

$T_{top} = 20 \text{ ns}$

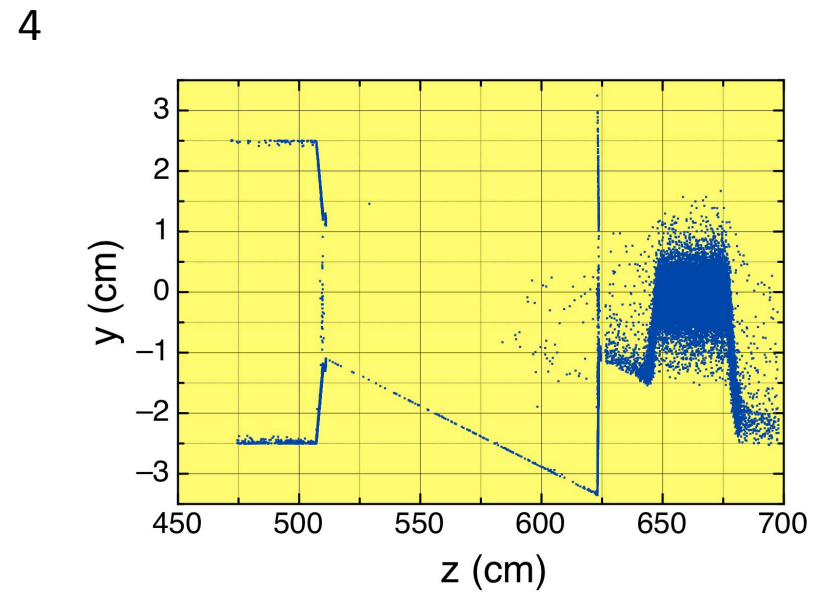
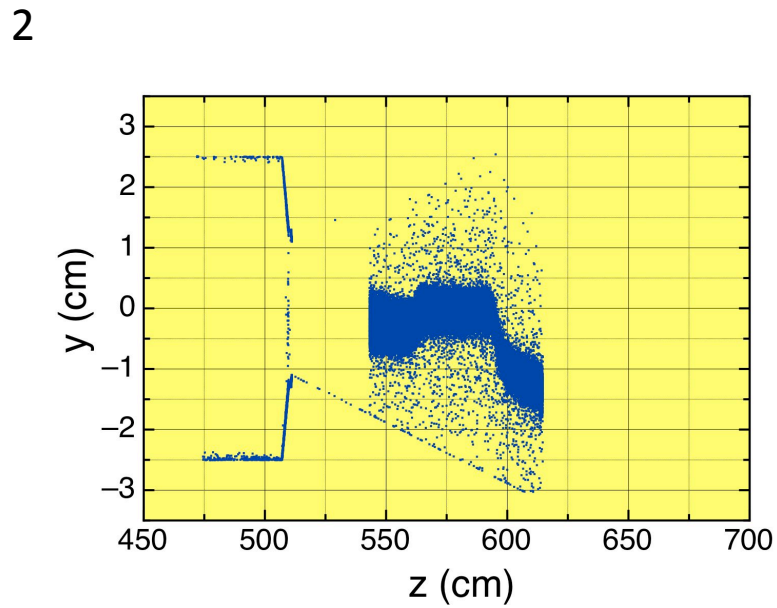
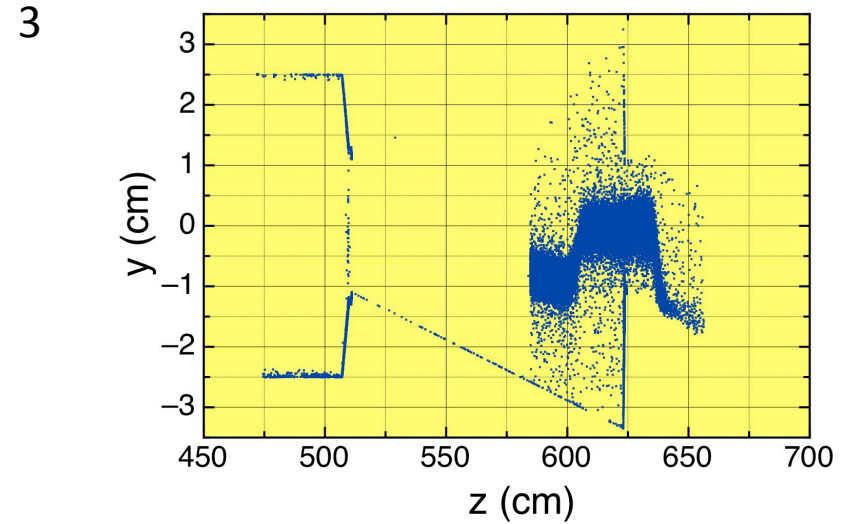
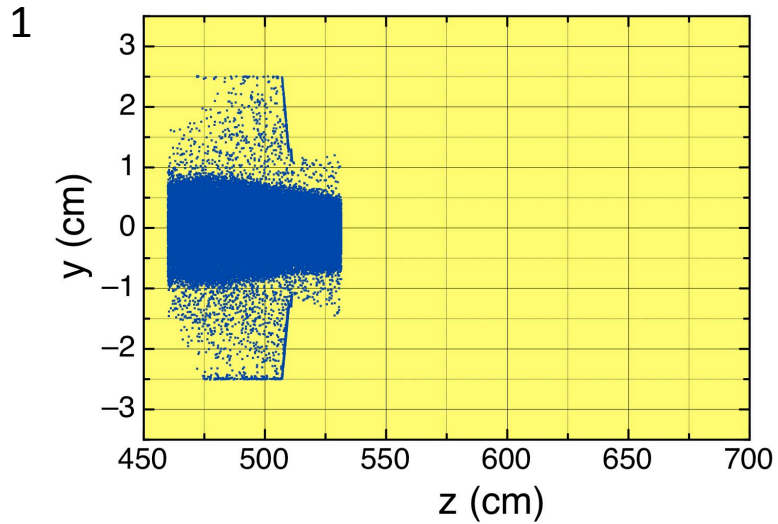
$T_{front} = 10 \text{ ns}$

Long pulse beam

$T_{top} = 280 \text{ ns}$

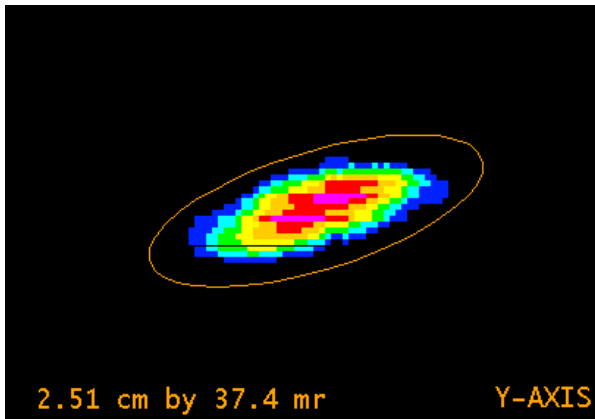
$T_{front} = 10 \text{ ns}$

BEAMPATH Simulation of LANSCE Beam Chopping

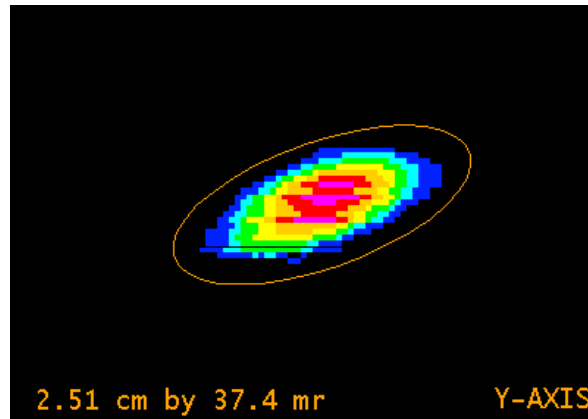


Effect of LANSCE Chopper Pulse Length on Beam Emittance

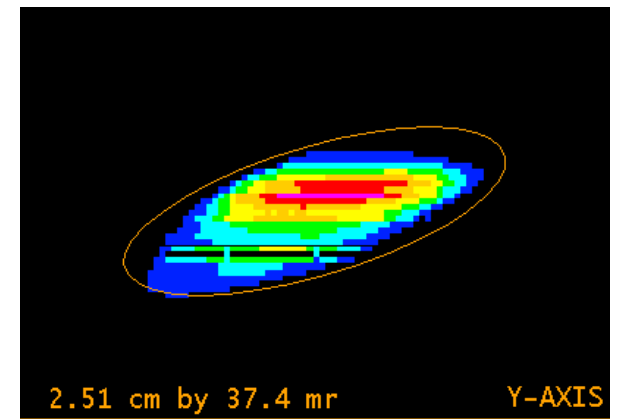
Chopper Off



Chopper pulse 290 ns



Chopper pulse 36 ns



Different Chopping Options for LEBT (C.Plostinar, ESS/AD/0022)

Table 1. LEBT and MEBT chopper parameters at CERN, J-PARC, RAL and SNS.

Chopper Location	CERN		J-PARC		SNS		RAL
	LEBT	MEBT	LEBT	MEBT	LEBT	MEBT	MEBT Only
Deflector Type	Electro-static	Electro-static	Induction Cavity	RF Cavity	Electro-static	Electro-static	Electro-static
Deflector Type Details	Deflecting plate	Meander Stripline	Beam Transformer	TE11 Mode	Einzel Lens	Meander Stripline	Stripline with Coaxial/Stripline Delay
Beam Energy	45 keV	3 MeV	~50 keV	3 MeV	65 keV	2.5 MeV	3 MeV
Beam Pulse Length	0.4 ms		0.5 ms		1 ms		2 ms
Repetition Rate	50 Hz		25 Hz		60 Hz		50 Hz
Bunch Frequency	-	352.2 MHz	-	324 MHz	-	402.5 MHz	324 MHz
Rise Time	2 μ s	2 ns	<50 ns	10 ns	<50 ns	10 ns	2 ns
Bunch by bunch chopping	-	Yes	-	No	-	No	Yes
Deflector Length	10 cm	2*40 cm	10 cm	17.2 cm	2.7 cm	2* 35 cm	2* 45 cm
Deflecting Voltage/Field	< 20 kV	+/- 600 V	+/-2.5 kV	1.6 MV/m	+/- 3 kV	2.5 kV	+/- 1.5 kV

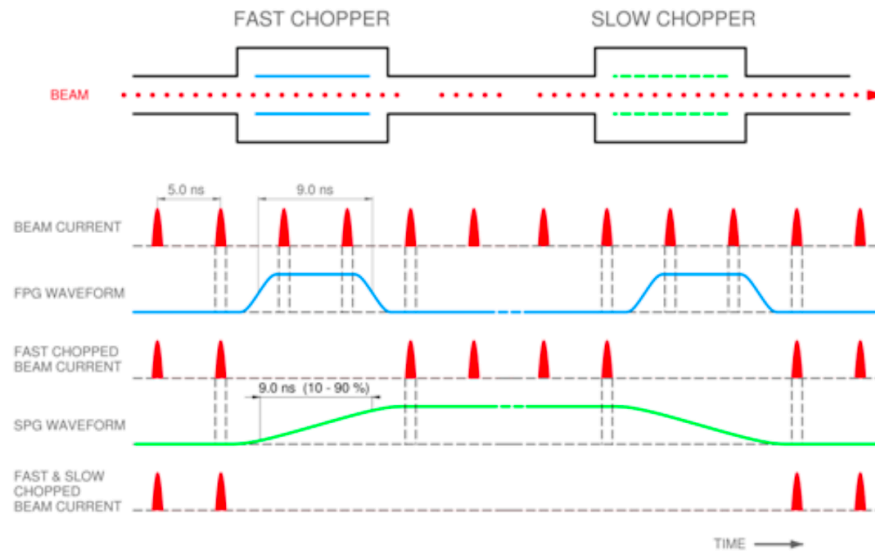
As mentioned above, because of the rise and fall times of the chopper voltage in the LEBT (tens of ns), the beam will contain partially chopped bunches. These bunches have a trajectory which is to some extent rather uncertain and are likely to be lost along the linac. To mitigate this effect, CERN, J-PARC and SNS combine the “slow” chopper in the LEBT with a fast MEBT chopper.

A TWO STAGE FAST BEAM CHOPPER FOR NEXT GENERATION HIGH POWER PROTON DRIVERS

Michael A. Clarke-Gayther, STFC RAL, Didcot, United Kingdom



RAL 'Fast-Slow' two stage chopping scheme



The upstream field is generated by a pair of AC coupled 'fast' transition time pulse generators (FPG) that output high voltage, dual polarity pulses into a 'slow-wave' transmission line electrode structure [2], where partial chopping of beam bunches is avoided by ensuring that the deflecting E-field propagates at the beam velocity. The

3.0 MeV MEBT Chopper (RAL FETS Scheme A)

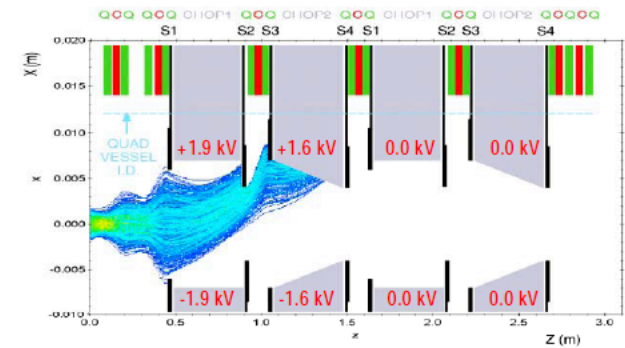
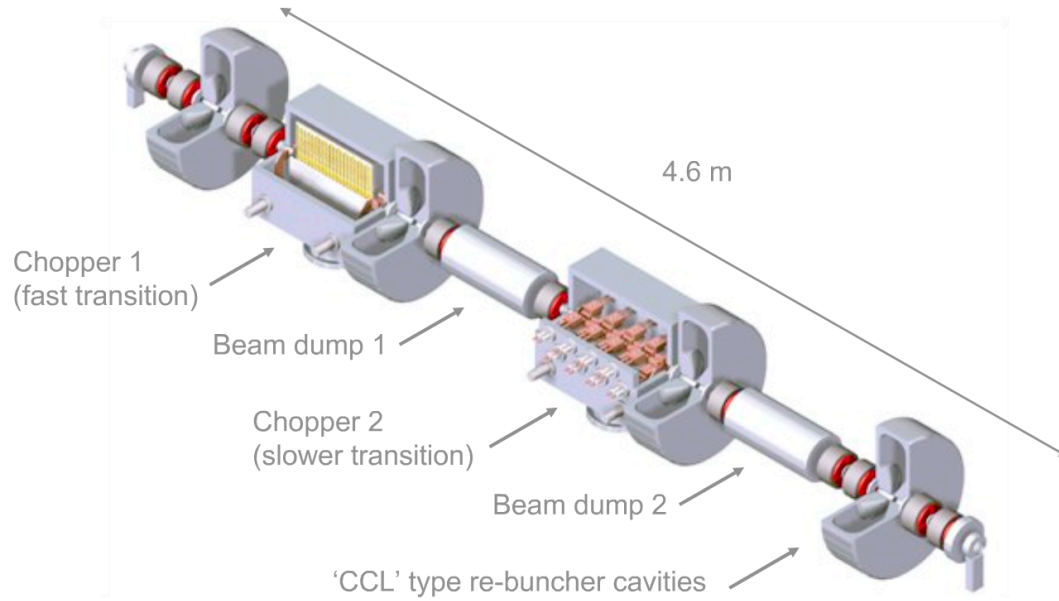


Figure 5: Fast chopping / Bunch 1-3 and 63-66 chopped.

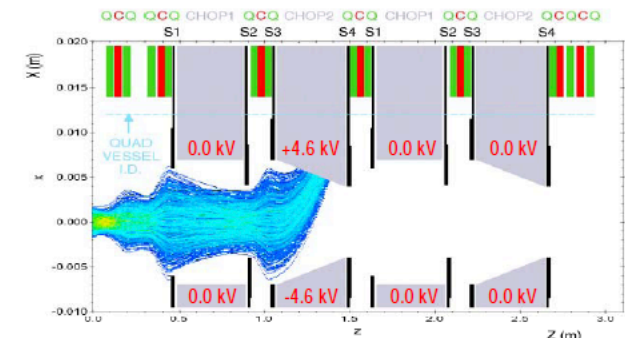


Figure 6: Slow chopping / Bunch 4-62 chopped.

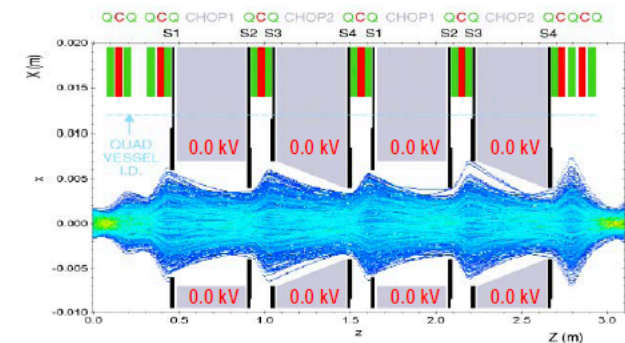


Figure 7: No chopping / Bunch 67-158 un-chopped.

CERN LEBT Pre-Chopper

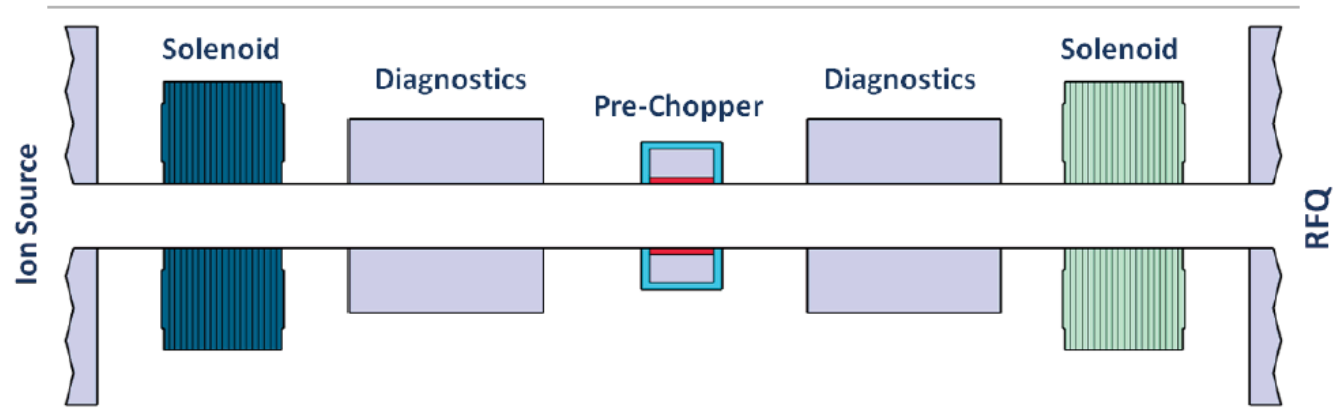
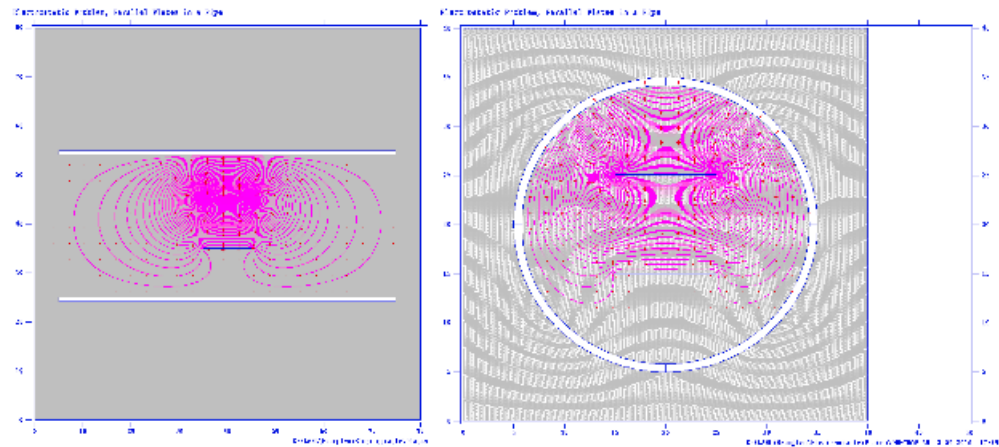
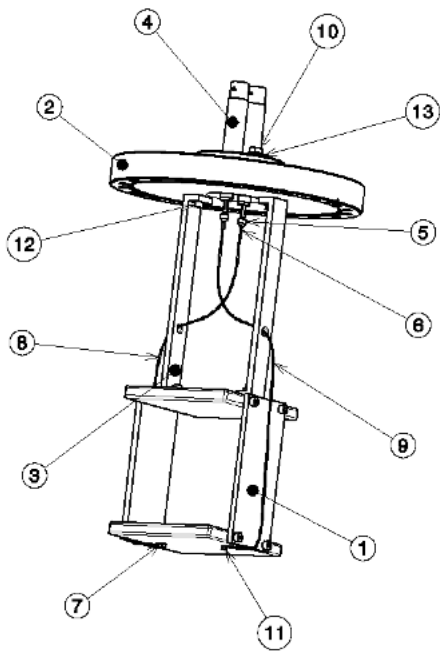
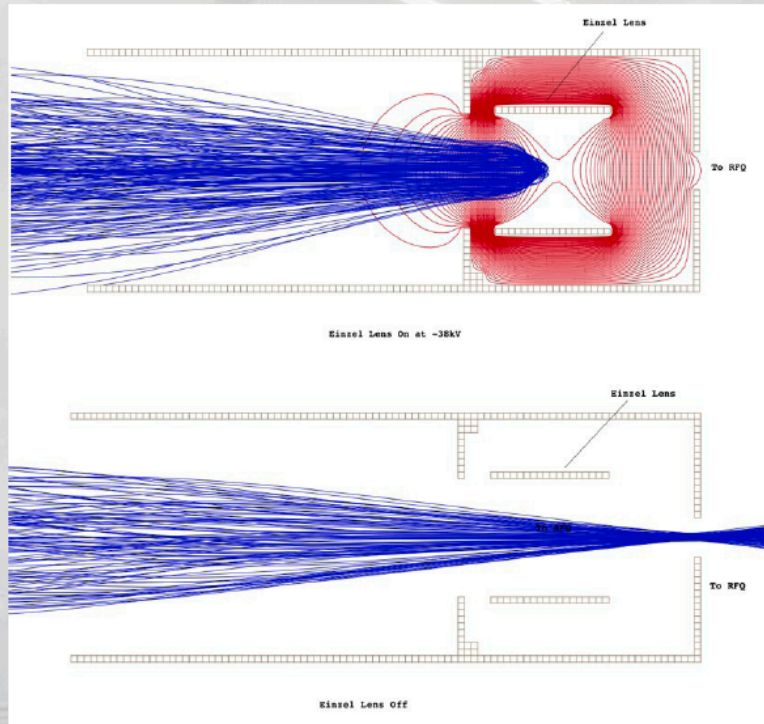


Figure 3: Schematic layout of the CERN Linac4 LEBT line.

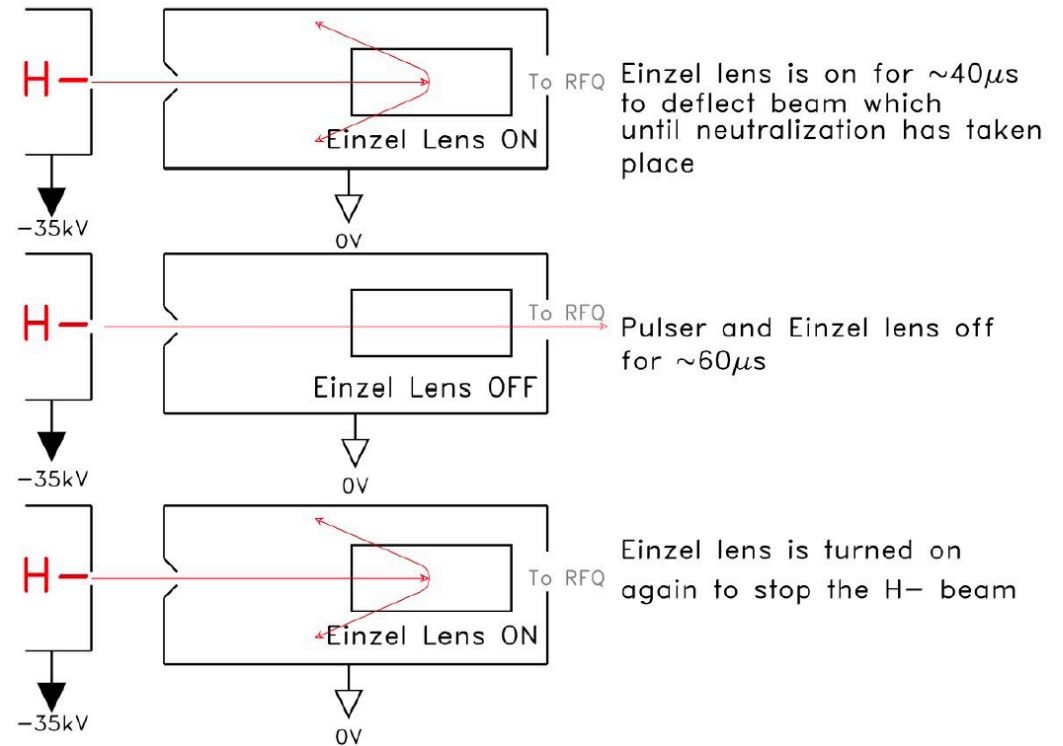


FNAL Einzel Lens Chopper

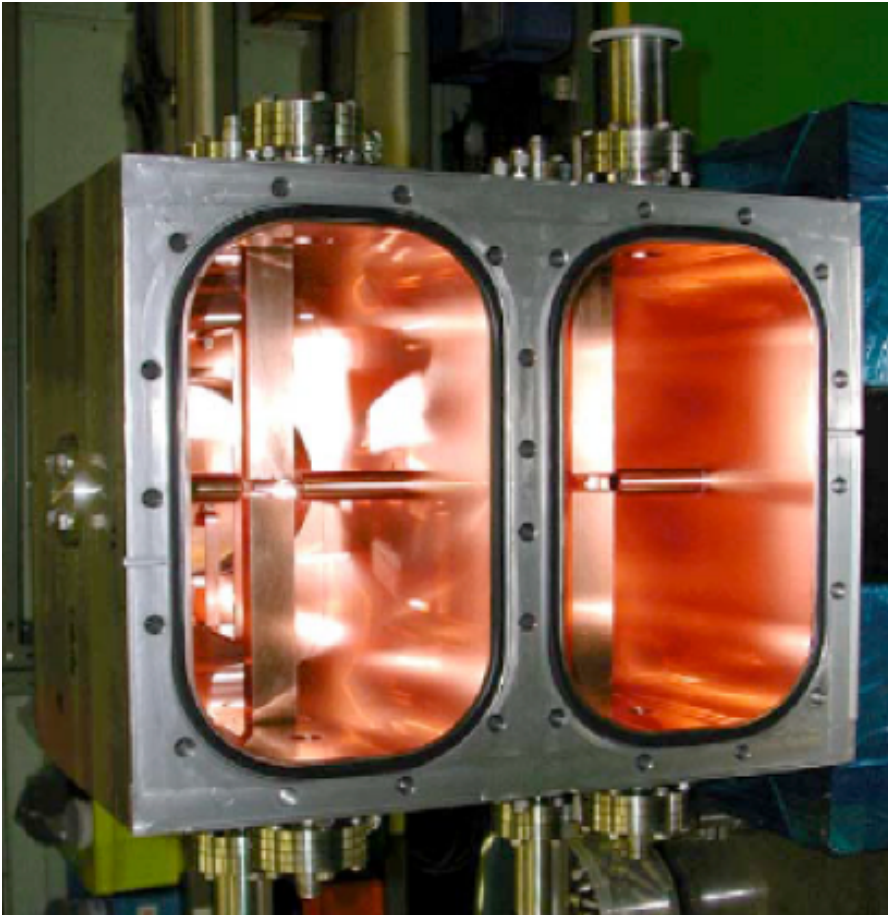
Einzel Lens Chopper



- Simulation using SIMION
- Optimized lens
 - 2" long
 - 1.75" diameter
 - -37 kV to stop 35keV

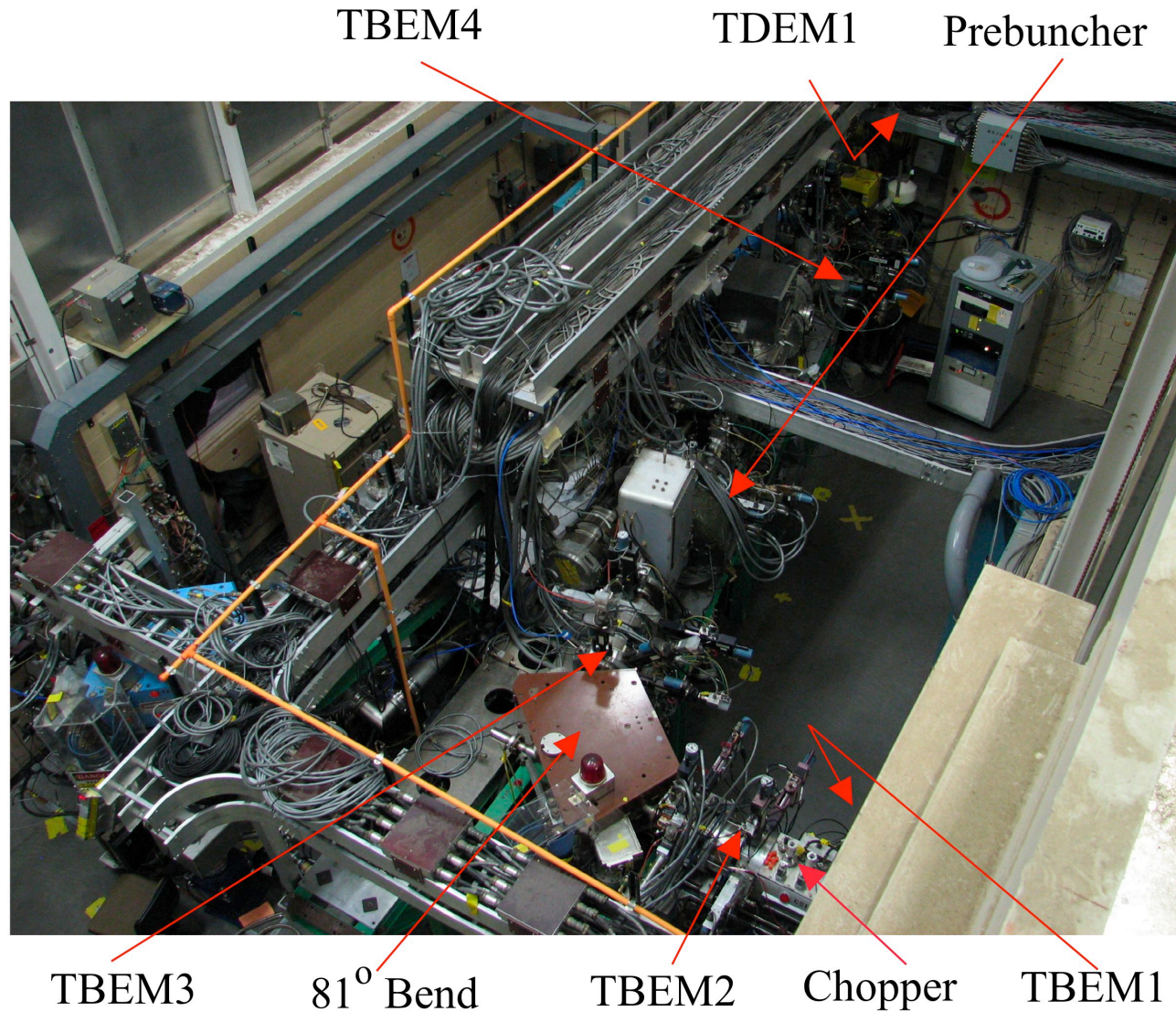


J-PARC RF Deflector

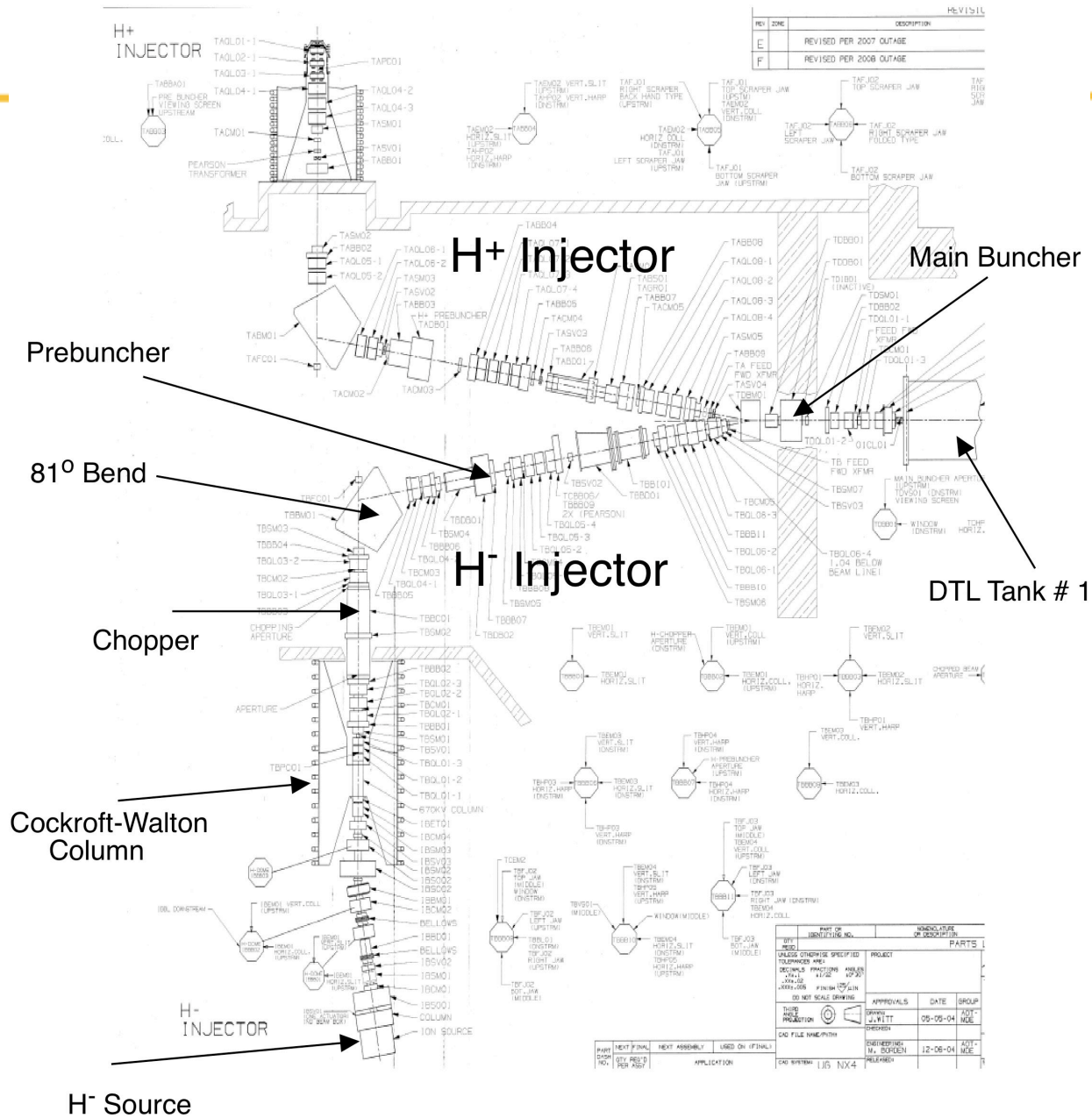


frequency	324 MHz
Q	~10
Cavity rise time	10ns
Power amplifier	Solid state, 36kW
Amplifier rise time	15ns
Max field	1.6MV/m
Gap length	20mm

Beam Matching in LEBT



LANSCE 750 keV H⁻ Low Energy Beam Transport



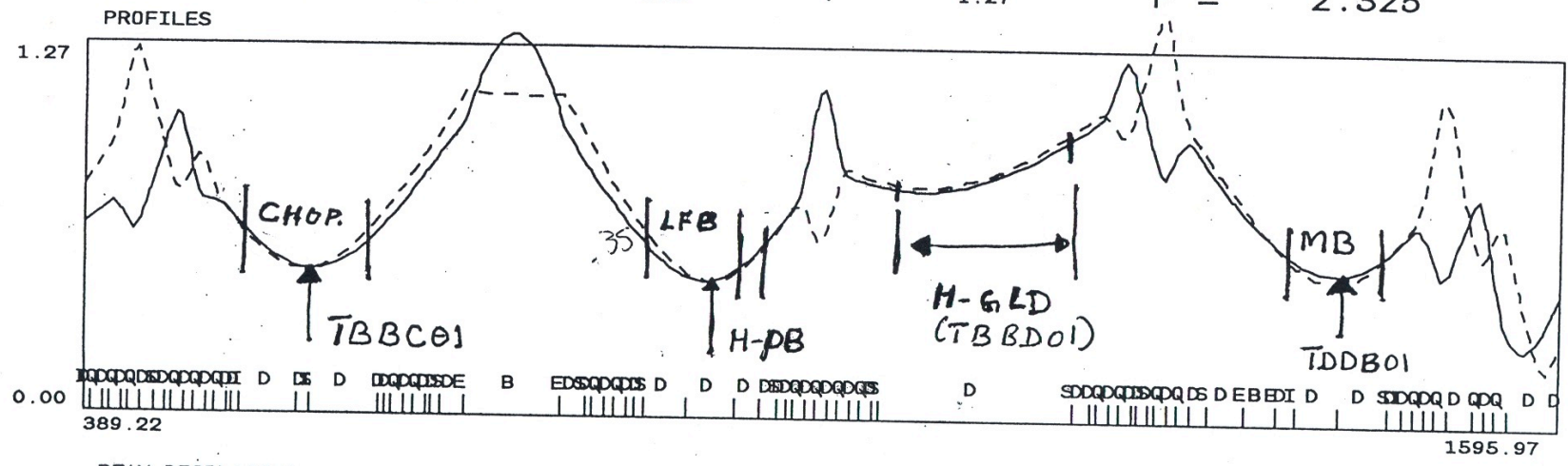
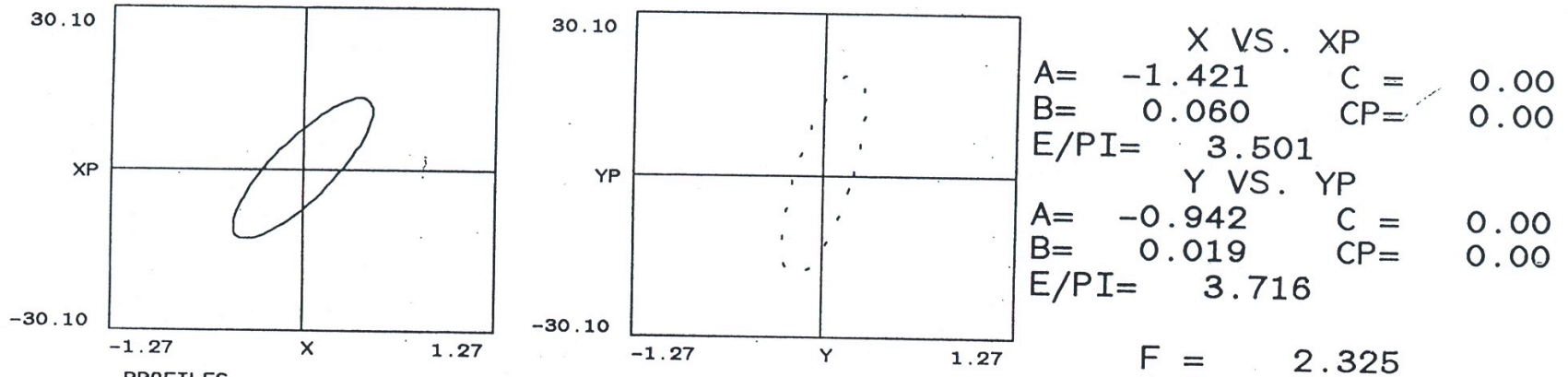
REV	ZONE	DESCRIPTION
E		REVISED PER 2007 OUTAGE
F		REVISED PER 2008 OUTAGE

PART OF IDENTIFYING NO.		MINIATURE OR DESCRIPTION	
BY:	REV:	DATE:	PROJECT:
UNLESS OTHERWISE SPECIFIED TOLERANCES ARE:			
FINISH:	ASSEMBLY:	DATE:	SCALE:
DO NOT SCALE DRAWING			
DATE:	APPROVALS:	DATE:	GROUP:
PRODUCTION:	J. WITT	05-05-04	207
CAD FILE NAME/PATH:		DESIGNER:	DATE:
		M. BORDEN	12-06-04
		RELEASED:	SCALE:
			1:1

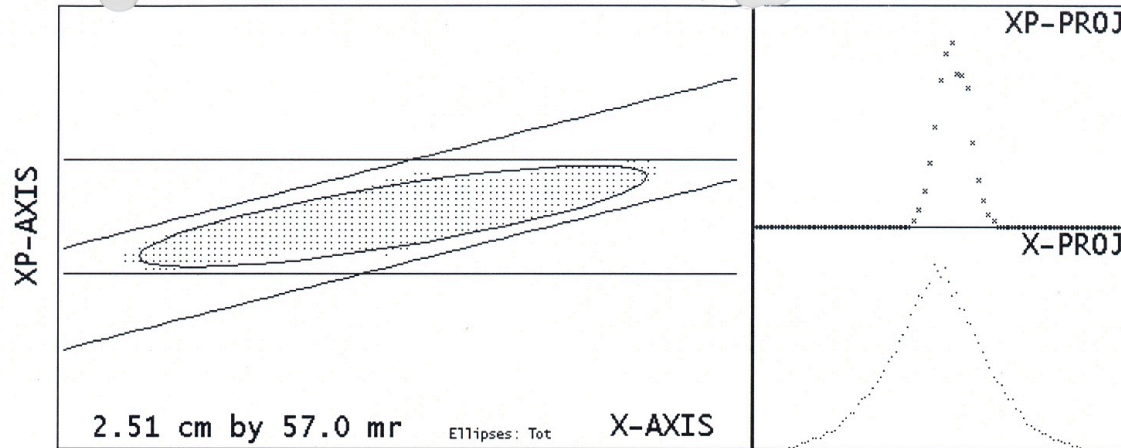
750 keV LANL injector of H+ / H- Beams

Matching of the H⁻ Beam with 750 keV Low Energy Beam Transport

TRACE TRACE 20-FEB-96 13:52:37 LCS_DAT [LCSA.TRACE]CP1.TRA
 N1= 3. I2=146 I= 1.00 SC=T W= 0.750 X= 5.

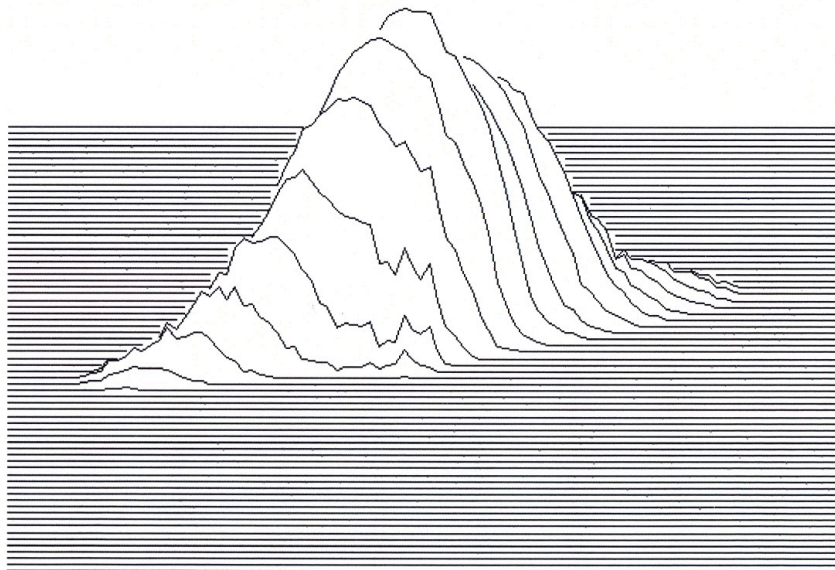


Emittance Scans for Beam Matching



E = 750.0 KeV
 b*g = 0.04000
 Polarity: +
 Scale: 1 mA
 File:
 /epics/1cs/data/em/
 console/emldata.24540

*D-BG D = 670
 L = 160*



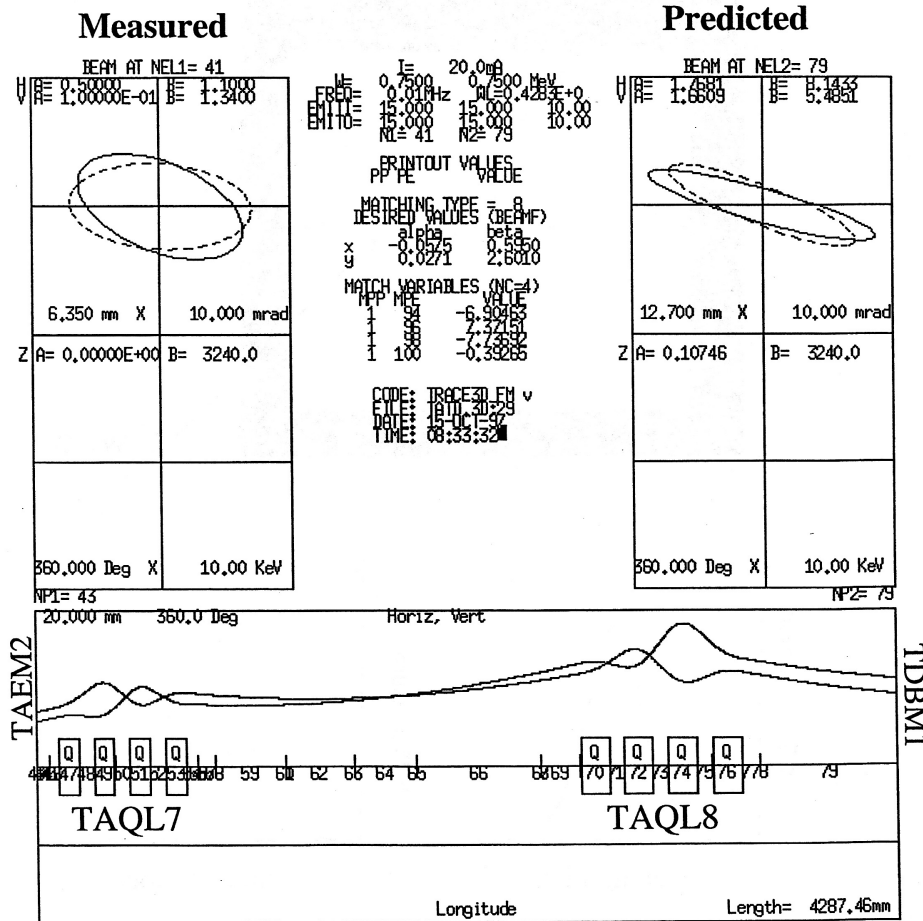
```

Run: 24540      Stn: TBEM01-H
02:38:38      09-Sep-2013
Beam: H-      Meas, Norm
E(total) = 3.838, 0.154 pi
E(edge) = 3.534 pi
E(rms) = 0.476, 0.019 pi
Etot/rms = 8.07
Alpha = -1.309
Beta = 0.230
4*E(rms) = 1.902 pi
C = -0.041 cm
CP = 1.478 mr
X Sigma = 0.3306 cm
XP Sigma = 2.3700 mr
Thold = 2.0 %, 10 cnts
Maximum Counts = 523
Beam thru thresh = 81532
Total Beam = 82904
Slit Pos = 866 1092
Clctr Pos = 1256 1837
Slit Rate = 93, Nom. = 80
Clctr Rate = 238, Nom. = 224
E(ea) = 6.126, 0.245 pi
E(ea)/E(rms) = 12.881
    
```

Beam Matching Using Envelope Code

Use of Emittance Measurements

- Measure the beam Emittance and Twiss Parameters at one point.
- Using a simulation code we can then predict the trajectory of the beam envelope through a region to a point where the beam cannot be measured.



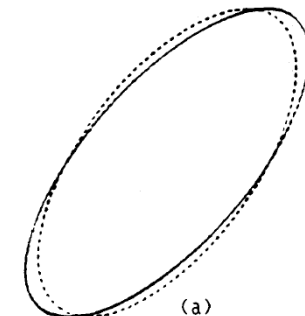
Mismatch factor between expected and actual beam

$$F = \sqrt{\frac{1}{2}(R + \sqrt{R^2 - 4})} - 1$$

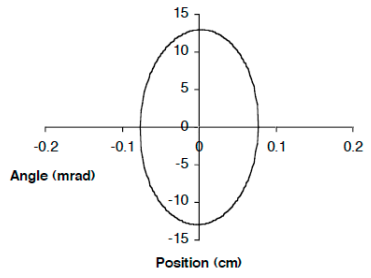
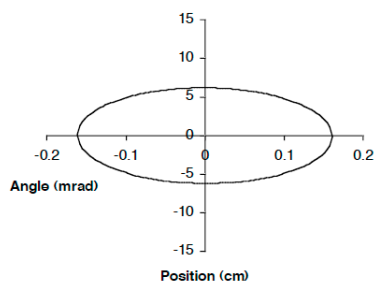
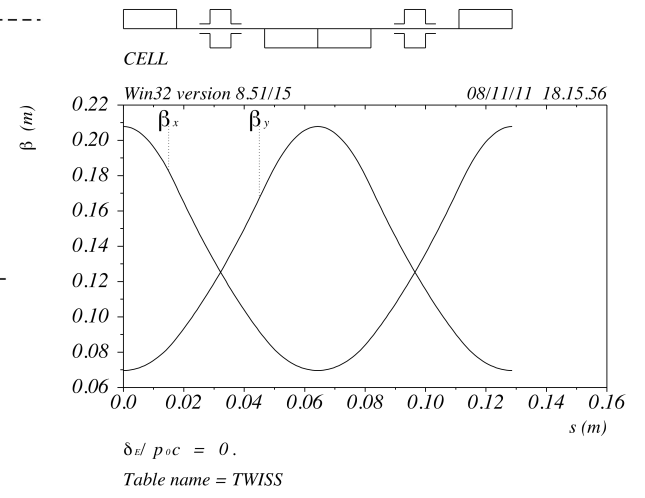
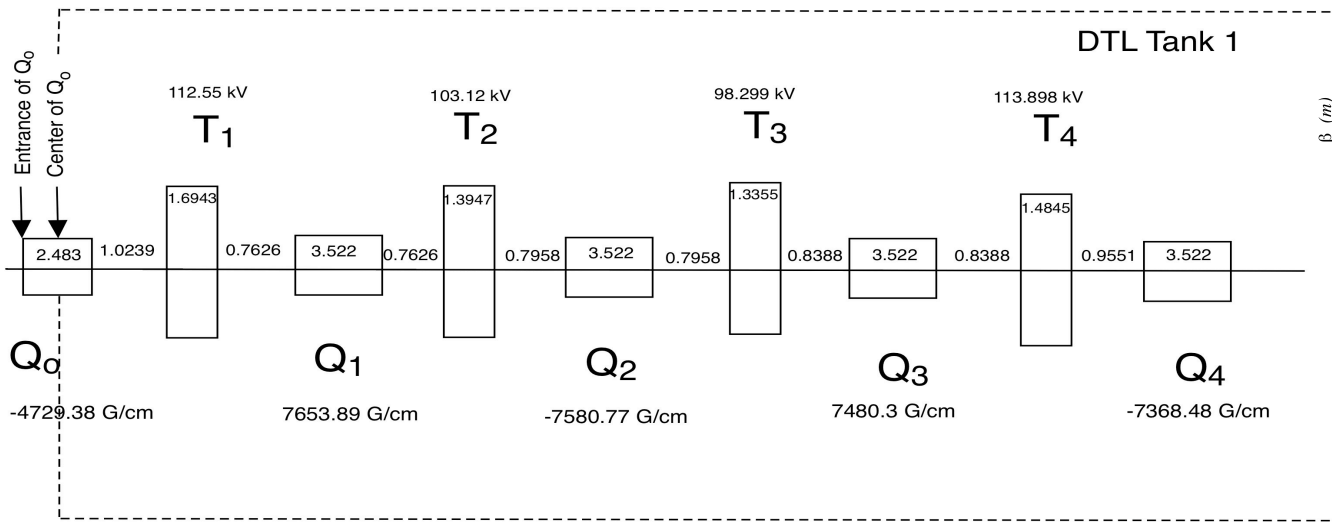
$$R = \beta_{\text{exp}} \gamma_s + \beta_s \gamma_{\text{exp}} - 2\alpha_{\text{exp}} \alpha_s$$

Average mismatch

$$\bar{F} = \frac{1}{2}(F_x + F_y)$$



Beam Matching at the Entrance of LANL DTL



Matched beam ellipses at the entrance of DTL

Phase advance per cell

$$\mu_o = \frac{L}{2D} \sqrt{1 - \frac{4D}{3L} \frac{qG_m D^2}{m\gamma\beta c}} = 0.9749 \quad (55.8^\circ)$$

Max value of beta-function

$$\beta_{\max} = \frac{L(1 + \sin \frac{\mu_o}{2})}{\sin \mu_o} = 21.3 \text{ cm}$$

Min value of beta-function

$$\beta_{\min} = \frac{L(1 - \sin \frac{\mu_o}{2})}{\sin \mu_o} = 7.716 \text{ cm}$$

Unnormalized acceptance

$$A = \frac{a^2}{\beta_{\max}} = \frac{a^2}{L} \frac{\sin \mu_o}{(1 + \sin \frac{\mu_o}{2})} = 26.4 \pi \text{ cm mrad}$$

Normalized acceptance

$$\epsilon_{\text{accept}} = \beta\gamma A = 1.056 \pi \text{ cm mrad}$$